Draft version August 16, 2016
Preprint typeset using LaTeX style emulateapj v. 05/12/14

arXiv:1410.7394v2 [astro-ph.GA] 15 Aug 2016

THE EVOLUTION OF POST-STARBURST GALAXIES FROM $Z \sim 1$ TO THE PRESENT

Petchara Pattarakijwanich[1,*,†], Michael A. Strauss[1], Shirley Ho[2], Nicholas P. Ross[3]

Draft version August 16, 2016

ABSTRACT

Post-starburst galaxies are in the transitional stage between blue, star-forming galaxies and red, quiescent galaxies, and therefore hold important clues for our understanding of galaxy evolution. In this paper, we systematically searched for and identified a large sample of post-starburst galaxies from the spectroscopic dataset of the Sloan Digital Sky Survey (SDSS) Data Release 9. In total, we found more than 6000 objects with redshifts between $z \sim 0.05$ and $z \sim 1.3$, making this the largest sample of post-starburst galaxies in the literature. We calculated the luminosity function of the post-starburst galaxies using two uniformly selected subsamples: the SDSS Main Galaxy Sample and the Baryon Oscillation Spectroscopic Survey CMASS Sample. The luminosity functions are reasonably fit by half-Gaussian functions. The peak magnitudes shift as a function of redshift from $M \sim -23.5$ at $z \sim 0.8$ to $M \sim -20.3$ at $z \sim 0.1$. This is consistent with the downsizing trend, whereby more massive galaxies form earlier than low-mass galaxies. We compared the mass of the post-starburst stellar population found in our sample to the decline of the global star-formation rate and found that only a small amount ($\sim 1\%$) of all star-formation quenching in the redshift range $z = 0.2 - 0.7$ results in post-starburst galaxies in the luminosity range our sample is sensitive to. Therefore, luminous post-starburst galaxies are not the place where most of the decline in star-formation rate of the universe is happening.

Keywords: Galaxies: Distance and Redshift — Galaxies: Evolution — Galaxies: High-Redshift — Galaxies: Luminosity Function — Galaxies: Starburst

1. INTRODUCTION

Post-starburst galaxies were first identified by Dressler & Gunn (1983) as a distinct class of galaxies, whose main spectroscopic characteristics are strong Balmer absorption lines with a lack of emission lines due to star formation. The physical explanation of these properties is that these galaxies had a large burst of star formation about 10^{8-9} years before the time of observation that suddenly was quenched, with very little ongoing star formation. This stellar population is old enough that the short-lived O- and B-stars have all died (thus no nebular emission lines), and young enough that the optical spectrum is dominated by A-stars (thus the strong Balmer absorption). Given the stellar population properties, one possible explanation is that these objects are in a transitional stage between star-forming blue cloud galaxies and quiescent red sequence galaxies.

The global star formation rate over the entire universe is found to have dropped by about an order of magnitude since redshift $z \sim 1$ (Madau & Dickinson 2014). This implies that the galaxy population changed drastically between redshift $z \sim 1$ and the present time. The heavily star-forming galaxies that are abundant at high redshift must be quenched and evolve to the red, passive elliptical galaxies. If this quenching is sudden, then they will pass through the post-starburst phase in between. Therefore, we expect that the post-starburst galaxy population in this redshift range would reflect this change in the global star formation rate. In order to understand this, one needs a large, statistical sample of post-starburst galaxies that are selected with a uniform and well-understood selection method across this large range of redshift.

The terminology in post-starburst galaxy studies is rather rich and confusing. Two common names are "K+A" and "E+A", referring to the fact that the spectra of this kind of galaxy can be decomposed into spectra of "K"- and "A"-stars (and "E" stands for elliptical galaxy, whose spectrum is dominated by K-giants). Some authors have also defined a number of subclasses such as E+a (Choi et al. 2009) and post-quenching (Quintero et al. 2004). They are also closely related to the "green valley" galaxies, lying intermediate between the red sequence and blue cloud, although not all green valley galaxies have the spectroscopic signature of post-starburst galaxies. In this paper, we will use a specific working definition of post-starburst galaxies based on quantities measured from optical spectra, but otherwise we will make no particular distinction between these names and just call such objects collectively as "post-starburst".

Two main scenarios have been proposed to explain the formation of post-starburst galaxies, which predict different detailed properties of these galaxies. While it is likely that both mechanisms contribute to the formation of post-starburst galaxies to some degree, the relative importance of the two mechanisms is far from clear. Moreover, the relative importance of each mechanism can potentially be a function of redshift and galaxy mass.

[1] Department of Astrophysical Sciences, Princeton University, Peyton Hall, 4 Ivy Lane, Princeton, NJ 08544, USA
[2] McWilliams Center for Cosmology, Department of Physics, Carnegie Mellon University, 5000 Forbes Avenue, Pittsburgh, PA 15212
[3] Department of Physics, Drexel University, 3141 Chestnut Street, Philadelphia, PA 19104, USA
[*] Currently a KIAA Postdoctoral Fellow at the Kavli Institute for Astronomy and Astrophysics, Peking University, 5 Yi He Yuan Road, Hai Dian District, Beijing, 100871, China
[†] ppattara@pku.edu.cn

The first scenario is a cluster-related mechanism such as ram-pressure stripping. In this picture, gas-rich star-forming galaxies fall into galaxy clusters and their gas is removed by the interaction with the hot intracluster medium, suddenly quenching their star formation (Gunn & Gott 1972; Balogh et al. 2000). According to this scenario, the resulting post-starburst galaxies would be found predominantly in dense environments such as galaxy groups and clusters. They would still resemble disk galaxies, since nothing apart from gas loss would disturb their morphologies. This idea was first proposed by Dressler & Gunn (1983) because the first post-starburst galaxies they found were in clusters, and they therefore hypothesized that these objects lay exclusively in overdense regions. It was only found later that these objects are also present in the field (Zabludoff et al. 1996; Quintero et al. 2004; Blake et al. 2004). Interaction with the intra-cluster medium is also proposed as a possible way to form S0 galaxies.

An alternative scenario is that post-starburst galaxies are associated with galaxy interactions, mergers or AGN feedback. In this scenario, when gas-rich galaxies go through a merger phase, the gas is disturbed and collapses to form stars, leading to a large scale starburst. The same disturbance also funnels the gas to the galactic center, resulting in both a central starburst and AGN activity. The galaxy then either runs out of gas and stops forming stars, or the rest of the gas receives enough heating from either supernova or AGN feedback that it becomes too hot to collapse further or is expelled altogether. Either way, the galaxy goes through a starburst phase that stops quickly. This picture makes a number of predictions about the properties of post-starburst galaxies. The first is that it naturally explains the observations of post-starburst galaxies in lower density regions such as poor groups and the field. Their morphologies should show prominent signs of recent interactions such as tidal tails (Zabludoff et al. 1996; Yang et al. 2004, 2008; Blake et al. 2004; Tran et al. 2004; Goto 2005). Post-starburst galaxies are also expected to generally coincide with AGN, since both starburst and AGN activity are likely triggered by the same mechanisms. Also, the post-starburst stellar population is predicted to be centrally concentrated in their galaxies because the gas is driven toward the center in a merger, making the post-starburst galaxies appear more compact than elliptical galaxies at similar redshift. Observations show that this indeed is the case (Pracy et al. 2012; Swinbank et al. 2011; Whitaker et al. 2012).

The picture that gas-rich mergers drive both star formation and AGN activity is supported by theoretical work as early as, for example, Sanders et al. (1988) and Mihos & Hernquist (1994). More recent simulation papers that study this scenario include, for example, Hopkins et al. (2006, 2008); Bekki et al. (2001, 2005, 2010) and Snyder et al. (2011). Their models suggest that the spectrum of a merging system starts with strong Balmer absorption with a moderate amount of emission lines, then goes through a post-starburst phase when the emission lines fade out. After about 1 Gyr, the galaxy becomes dominated by an old stellar population.

There are also other models that attempt to explain this post-starburst phenomenon. Poggianti & Wu (2000) and Miller & Owen (2001) suggest that post-starburst galaxies are in fact dust-enshrouded starburst galaxies. In this picture, the ongoing star formation is hidden behind a large amount of dust and gas and therefore the emission lines are completely extincted. Balmer absorption lines, on the other hand, originate from A-stars, which are long-lived enough to migrate out of the star-forming gas cloud and become visible. This idea can be tested at far-infrared or radio continuum wavelengths, at which one can measure the star formation rate independent of dust and gas extinction. Various authors have carried out this test and the conclusion is that even though a small number of post-starburst galaxies may include dust-enshrouded starbursts, this model does not explain the majority of the post-starburst galaxy population (Miller & Owen 2001; Goto 2004; Chang et al. 2001; Nielsen et al. 2012).

In order to study post-starburst galaxies and understand the relative importance of different star-formation quenching mechanisms, the first important task is the selection of the sample itself. Post-starburst galaxies are typically selected spectroscopically, with the requirement that the Balmer absorption be strong. The Hδ line is commonly used for this purpose because emission from star formation tends to be quite weak in this line, unlike Hα or Hβ. It also does not have other major lines in its immediate vicinity, making the equivalent width measurement easy. The nebular emission lines, commonly represented by Hα and [OII]3727, are required to be weak. For objects at higher redshift, Hα drops out of the wavelength coverage of optical instruments and therefore the selection is usually done on the Hδ and [OII] lines alone. There are also a number of alternative methods such as spectral template fitting (Quintero et al. 2004), Principal Component Analysis (Wild et al. 2007, 2014) and using UV-optical colors (Choi et al. 2009).

A large sample is important to statistically represent the whole population. Large spectroscopic surveys have enabled the selection of samples of post-starburst galaxies containing hundreds of objects at low redshift (Zabludoff et al. 1996; Goto 2005, 2007; Wild et al. 2007; Quintero et al. 2004), and a few tens at higher redshift (Blake et al. 2004; Yan et al. 2009; Vergani et al. 2010), compared to a handful of objects in earlier studies. With these samples, various global properties of the samples have been studied, such as the luminosity function (Blake et al. 2004), their clustering (Krause et al. 2013) and quantification of their environments (Zabludoff et al. 1996; Galaz 2000; Blake et al. 2004; Balogh et al. 2005; Hogg et al. 2006; Yan et al. 2009; Poggianti et al. 2009).

More detailed information can also be obtained for a small number of post-starburst galaxies through follow-up observations. Detailed morphological studies using HST have been carried out by Belloni (1997); Caldwell et al. (1999); Tran et al. (2003, 2004); Blake et al. (2004); Yang et al. (2004, 2008) and Cales et al. (2011), who have shown that they show a range of morphologies. Spatially resolved spectroscopic data, either through long slit or integral field units, have been obtained and used to study the dynamical properties (Caldwell et al. 1996) and the spatial distribution of the post-starburst stellar population in individual galaxies (Norton et al. 2001; Goto 2005; Yagi & Goto 2006; Pracy et al. 2005, 2009, 2010, 2012; Goto et al. 2008; Swinbank et al. 2011).

In this paper, we tackle this rich and complicated problem at the key limitation of previous studies - small sample size - by first identifying a large number of post-starburst galaxies from the Sloan Digital Sky Survey (SDSS) database over a very broad range of redshift. In Section 2 we introduce the SDSS data, and give some technical background. In Section 3 we describe the method used to identify the post-starburst galaxies from this large spectroscopic dataset. The properties of the resulting sample is then described in Section 4. The luminosity function analysis of this sample, and its relation to the global star-formation rate, are then explained in Section 5. The discussion and conclusion of the results are then presented in Sections 6 and 7.

2. DATA

2.1. *SDSS and BOSS Surveys*

The Sloan Digital Sky Survey (York et al. 2000) has taken both imaging and spectroscopic data over more than a quarter of the sky, using a dedicated 2.5m telescope situated at the Apache Point Observatory in New Mexico (Gunn et al. 2006). The imaging data are taken in the five-band filter system - *ugriz* - defined in Fukugita et al. (1996) with the mosaic CCD camera described in Gunn et al. (1998). The raw imaging data are processed, calibrated and cataloged by algorithms described in Lupton et al. (2001). A subset of detected sources are selected for spectroscopic follow-up by a number of selection criteria based on observed magnitudes and colors. These targets are then assigned to spectroscopic tiles (Blanton et al. 2003) and their spectra obtained with the spectrograph described in Smee et al. (2013). In the first two phases of the survey (SDSS-I, SDSS-II) the selection was concentrated into three categories: a magnitude-limited sample of galaxies; the Main Galaxy Sample (Strauss et al. 2002), luminous red galaxies (LRG) at higher redshift (Eisenstein et al. 2001) and quasars (Richards et al. 2002). Spectra obtained in these phases cover the wavelength range between $3800 - 9200$Å at resolution of $R \sim 2000$, with typical signal-to-noise ratio per resolution element > 4 for objects brighter than $g = 20.2$. The spectra are both wavelength- and spectrophotometry-calibrated. In the third phase of the survey, SDSS-III (Eisenstein et al. 2011), the BOSS program (Dawson et al. 2013) was carried out with an upgraded spectrograph (wavelength coverage $3600 - 10400$Å, with signal-to-noise ratio > 5 at $i = 21$). This program concentrated on galaxies and quasars at higher redshift for measurement of Baryon Acoustic Oscillations. The spectra observed are classified with redshifts measured by the spectral classification algorithm explained in Bolton et al. (2012). In addition, for the first two phases of the SDSS survey, an alternative spectral classification was performed (SubbaRao et al. 2002). In this work we based our study on all available spectra in SDSS-I/II and BOSS spectra in SDSS-III up to the Data Release 9 of the survey (SDSS DR9; Ahn et al. 2012).

2.2. *SDSS Magnitude System*

For each SDSS object, the inverse hyperbolic sine magnitude (asinh; Lupton et al. 1999) in the AB system in all five bands is measured from raw imaging data by a number of different methods, resulting in a variety of magnitudes that we will find ourselves using throughout this paper. Fiber magnitude measures the flux contained within the spectrograph fiber. Petrosian magnitude is designed to measure galaxy photometry optimally (Petrosian 1976; Blanton et al. 2001; Yasuda et al. 2001 and Strauss et al. 2002). The PSF magnitude measures the flux of a point source, using the PSF as a matched filter. Model and cModel magnitudes measure the flux of a galaxy by fitting surface brightness profiles to the image. The Spectro magnitude measures the brightness from the spectra, relying on the excellent spectrophotometric calibration of SDSS (Adelman-McCarthy et al. 2008). In later analysis, we distinguish and convert between these magnitude systems. More details on this can be found in the SDSS website `http://www.sdss.org/dr12/algorithms/magnitudes/`.

2.3. *Small Sample of Post-Starburst Galaxies*

We assembled a small sample of known post-starburst galaxies at both low and high redshift, which will be used to test and tune the selection criteria that we will introduce in subsequent sections. This sample contains the 564 low-redshift ($z_{\rm median} \sim 0.1$) post-starburst galaxies found in the 5th Data Release of the Sloan Digital Sky Survey (Adelman-McCarthy et al. 2007) by Goto (2007). This sample was selected from the main galaxy catalogue at redshift $z < 0.33$ such that the Hα line is well within the wavelength coverage of the spectra. It was selected by the equivalent width cuts Hδ EW $>$ 5.0Å, Hα EW > -3.0Å and OIIλ3727 EW > -2.5Å, where positive value of equivalent width corresponds to absorption and negative value to emission. We add to this about 100 intermediate- and high-redshift objects (redshift $z \sim 0.4 - 0.8$) that were mostly found serendipitously from visual inspection of SDSS and BOSS spectra.

3. SELECTION OF POST-STARBURST GALAXIES

3.1. *Spectral Templates*

The selection method we use is based on template fitting, following Quintero et al. (2004). In this section we describe the templates we use. As suggested by the name "E+A" or "K+A", these objects' spectra can be decomposed into a linear combination of the spectrum of an old stellar population (the "E" or "K" component), and the spectrum of an A-type star. We use the old stellar population template of Eisenstein et al. (2003). This is the composite spectrum of Luminous Red Galaxies in SDSS, which is dominated by the light of K-type giants. The spectrum of Vega (an A0V star) from Bohlin & Gilliland (2004) is used to represent the "A"-template. Both "K" and "A" templates are normalized such that the total fluxes over the wavelength range 3600-4400 Å are the same, as shown in Figure 1. We emphasize that this template fitting approach is only a crude fit to the underlying stellar population. A proper and more detailed analysis of the stellar populations in our sample will be carried out in future work.

3.2. *Selection Methods*

3.2.1. *Redshift Range Determination*

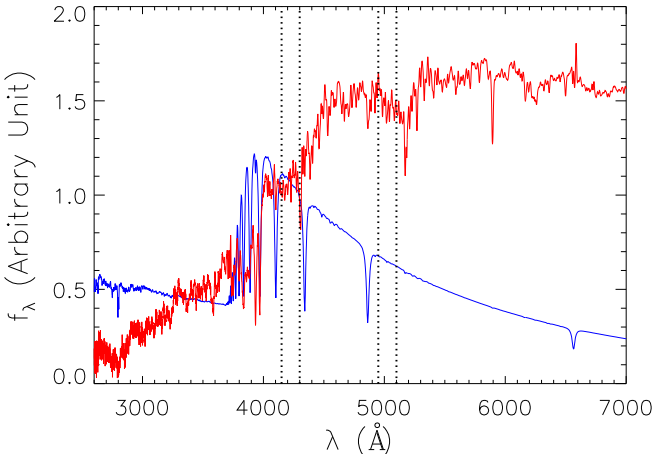

Figure 1. This plot shows the spectra used as fitting templates for "A" (blue) and "K" (red) components of the galaxy population. The "A"-template is the spectrum of Vega, which is representative of generic A0V stars, from Bohlin & Gilliland (2004). The "K"-template is the composite spectrum of Luminous Red Galaxies (LRGs) in SDSS (Eisenstein et al. 2003). The fits are carried over the wavelength range 3600-4400Å and the templates are normalized such that the integrated fluxes over this range are the same. The vertical dotted lines show the wavelength ranges 4150-4300Å and 4950-5100Å (hereafter called [4200] and [5000] respectively) corresponding to our fiducial bands used in later sections.

The SDSS main spectral classification pipeline provides redshifts and classifications for all spectra based on the Principal Component Analysis (PCA) technique (Bolton et al. 2012). This pipeline redshift is reliable for object types that are common and well represented in the PCA templates. This is not always the case for the post-starburst galaxies that we try to select, especially at high redshift. In the preliminary stage of this work we found that a number of known post-starburst galaxies, especially at high redshift, have wrong redshifts and are misclassified. Since we desire that the final sample be as complete as possible, we do not assume that the redshift value given by the pipeline is reliable, and will determine the redshift from the spectrum as if the redshift is not known a priori. For this reason we allow redshift to be a free parameter when we perform the template fitting. The redshift is constrained such that the rest-frame wavelength range of the template, 3600-4400Å, is contained within the observed spectra, corresponding roughly $z = 0.05 - 1.1$ for the SDSS wavelength coverage (3800-9200Å) and $z = 0 - 1.35$ for the BOSS wavelength coverage (3600-10200Å).

However, in SDSS-I/II, an alternative, independent spectral classification pipeline is available (SubbaRao et al. 2002). This pipeline disagrees in redshift with the main pipeline significantly for about 2% of the objects. Even though both of these pipelines can be individually incorrect, when the two agree the redshift is highly likely to be correct. So when this happens (more specifically, when the two redshifts differ by less than 0.005) we do not perform the template fitting over the full redshift range, but only around a narrow range $\Delta z = 0.008$ around the average of the two to find the local optimum. For BOSS, since this alternative pipeline is not available, the redshifts for BOSS galaxies are never assumed to be correct a priori (see the discussion in Section 4.3).

3.2.2. *Redshift Determination*

Once the redshift range to be fit over is determined, the template fitting is performed at every value of redshift in the range with uniform spacing $\Delta z = 0.001$. For each redshift value two models are fitted to the wavelength corresponding to 3600-4400 Å rest-frame wavelength, shifted to this value of redshift. The first model is to fit a linear combination of the "K"-template, "A"-template and a second-order polynomial in wavelength as continuum. This is written mathematically as

$$y_{\rm Model1} = C_K K(\lambda) + C_A A(\lambda) + C_0 + C_1\lambda + C_2\lambda^2 \quad (1)$$

where $K(\lambda)$ and $A(\lambda)$ correspond to the "K" and "A" templates. The continuum is included to take into account other possible slowly-varying effects such as AGN continuum, dust extinction, spectrophotometric errors and template errors. The second model is to fit only the second-order polynomial in wavelength, without the "K" and "A" templates.

For each fit, the value of the C parameters are determined by the standard minimum χ^2 fitting method, with each pixel weighted by the inverse square of the per-pixel error output by the spectroscopic pipeline. This method can yield negative, unphysical values of C_K or C_A. There are other classes of fitting method that can constrain parameters to be positive-definite. However, considering the ease of implementation and the fast computational speed (especially since we need to run this process on the whole SDSS and BOSS spectroscopic database, consisting of more than 2 million spectra), we use this simple χ^2 fit and tolerate this issue. This is not a problem since visual inspection (see below) is done at the end to ensure the quality of all fits anyway. Generally, it is also found that the polynomial component is usually small compared to the "K" and "A" components, thus the spectra are typically well represented by a linear combination of the two spectral templates.

For each redshift, we use the difference in χ^2 values of the two models, $\Delta\chi^2 = \chi^2_{\rm Model2} - \chi^2_{\rm Model1}$, as an indicator of a good template fit. $\Delta\chi^2$ indicates how much better the fit is for the model with templates included, compared to the pure polynomial model. A large value of $\Delta\chi^2$ could only happen if at least one of the "K" or "A" template is a good representation of the spectrum at that redshift. We take the redshift with the maximum value of $\Delta\chi^2$ as the true redshift of the object.

For true post-starburst galaxies we found that the value of $\Delta\chi^2$ is at least around 40-50 (much larger than $\Delta\chi^2 \sim 2$ expected by increasing the number of parameters by 2), and up to a few thousand for objects with strong post-starburst features with good signal-to-noise ratio. Values of $\Delta\chi^2$ lower than this are usually associated with low signal-to-noise spectra and it is usually unclear whether the post-starburst spectral features are actually detected, therefore they are removed in the visual inspection process.

3.2.3. *Identification of Post-starburst objects*

To quantify the contribution of the "A"-spectrum component to the fit in order to identify post-starburst

galaxies, we introduce a parameter, A/Total, defined as $A/(K+A+P)$ where K, A and P are the integrated fluxes in the wavelength range 4150-4300Å (hereafter called [4200]) of the "K", "A" and the polynomial components of the model fit described above. This wavelength range corresponds to the continuum between the two Balmer absorption lines Hγ and Hδ (Figure 1) which are prominent features in the A-star spectrum. We require that this A/Total ratio be greater than 0.25 for an object to be considered a candidate post-starburst galaxy. This particular cut at 0.25 is determined such that the selection algorithm recovers objects in the sample of known post-starburst galaxies (Section 2.3) with reasonably strong spectral features.

3.2.4. *Equivalent Width Cut; Visual Inspection*

We also put requirements, adopted from Goto et al. (2003), on the equivalent widths of two key spectral lines. We require that the rest-frame equivalent widths satisfy HδEW > 4.0Å and [OII]λ3727EW > -2.5Å, where a positive value in equivalent width corresponds to absorption. The requirement on strong Balmer absorption guarantees a substantial contribution from the A-star component, while the lack of [OII] emission indicates an insignificant amount of ongoing star formation. The requirement on the Hδ equivalent width is somewhat redundant with the requirement on A/Total ratio, since they both measure the contribution of the A-star component. We still include both to ensure that the high A/Total ratio is not only due to the good fit to the continuum by the A-star template. These cuts are less conservative than the cuts used in Goto (2007) (HδEW > 5.0Å). This choice is made so that the sample is as inclusive as possible before all candidates are visually inspected.

The equivalent widths are calculated by summing the flux density over the line. A linear function is fit to the red and blue sidebands of the line to define the continuum region, then the excess over this continuum in the line region is used to calculate the equivalent width. The values of rest-frame wavelengths used to define the red and blue sidebands and the bandpass of relevant lines (including Hα, which will be used in following sections) are shown in Table 1. We did not apply any cut on the signal-to-noise ratio of the equivalent width measurements. We will quantify the effects of limited signal-to-noise ratio when we derive the luminosity function in Section 5.

It should be noted that this selection method is designed to select only those post-starburst galaxies in which the starburst had occurred at least several tens Myr previously. Significantly younger post-starburst galaxies will have some [OII]λ3727 emission or weaker Hδ absorption, and thus can be excluded from the sample. We will discuss the effects of this incompleteness below.

Finally, after the fitting process and various cuts, we visually inspect the spectra of all candidate post-starburst galaxies. There is a fairly high false positive rate (objects that are flagged by the selection process as candidates, but turn out to be other classes of objects). Most of these are catastrophically wrong fits in which the templates happen to match to certain spectral features producing a (small) maximum value of $\Delta\chi^2$ at some assumed redshift while at the same time giving A/Total > 0.25. These objects are removed from the candidate list at this stage. The other class of contamination is A-stars and white dwarfs whose spectra fit the "A"-template extremely well at $z = 0$ by construction. This problem only exists for BOSS spectra because the wavelength coverage extends blue enough for the 3600-4400 Å range to be within the data coverage at zero redshift. We solve this issue by requiring the best-fit redshift to be bigger than $z = 0.02$, which vastly reduces the number of candidates to be visually inspected. The numbers of objects considered at each stage in the selection process are shown in Table 2. This selection method does a decent job of screening the entire spectroscopic database and selecting a relatively small number of potential candidates. Yet it still has a high false positive rate, about 300% for SDSS and 100% for BOSS, requiring human inspection of the spectra.

This selection method recovers most of the known post-starburst galaxies described in Section 2.3. More specifically, 452 objects out of 564 objects (∼80%) in the Goto (2007) sample are recovered. The ones that are not recovered are visually confirmed to either have signal-to-noise ratio too low or are simply contaminants to that sample. Therefore we believe that this selection method is robust and is able to identify most post-starburst galaxies in the sample, with a low false negative rate. It is not surprising that this selection method is robust when used against this known sample, since it was designed around this very sample. However, since the method is generic and the amount of fine-tuning is minimal, we expect that this selection method is robust in general.

4. SAMPLE PROPERTIES

In this section we present our final sample, which is distributed uniformly over the survey footprint as expected. An `ASCII` file containing the full list of post-starburst galaxies presented in this paper, along with important properties, is included. Table 3 shows example entries of that full list.

The redshift distributions of the post-starburst galaxies selected from both SDSS and BOSS are shown in Figure 3. The median redshifts are around 0.2 for SDSS and 0.6 for BOSS respectively, with very little overlap between the two samples. Example of the spectra of these objects are shown in Figure 4. These examples are selected to illustrate a range of properties spanned by the objects in our sample. A diverse range of spectral features are seen among the objects in this sample. First is the strong Balmer lines, especially Hδ, in absorption which is one of the requirements for the selection. A number of objects show a blue continuum blueward of 4000Å, which is a sign of either a young stellar population or AGN activity. A large number of objects show weak MgII absorption, some even with detectable blueshift, indicative of outflows, which may be driven by either an AGN or a compact starburst (Tremonti et al. 2007; Diamond-Stanic et al. 2012; Sell et al. 2014). More rare are objects with broad MgII in emission, clearly indicative of AGN activity. These are "post-starburst quasars" (for example, Brotherton et al. (1999, 2004)). The Hα line for lower-redshift objects also shows a diverse range of behaviors, ranging from absorption to broad line emission. This Hα behavior and how it is related to the contamination in the selection will be discussed in Section 4.4. The quantities A/Total and Hδ absorption Equiva-

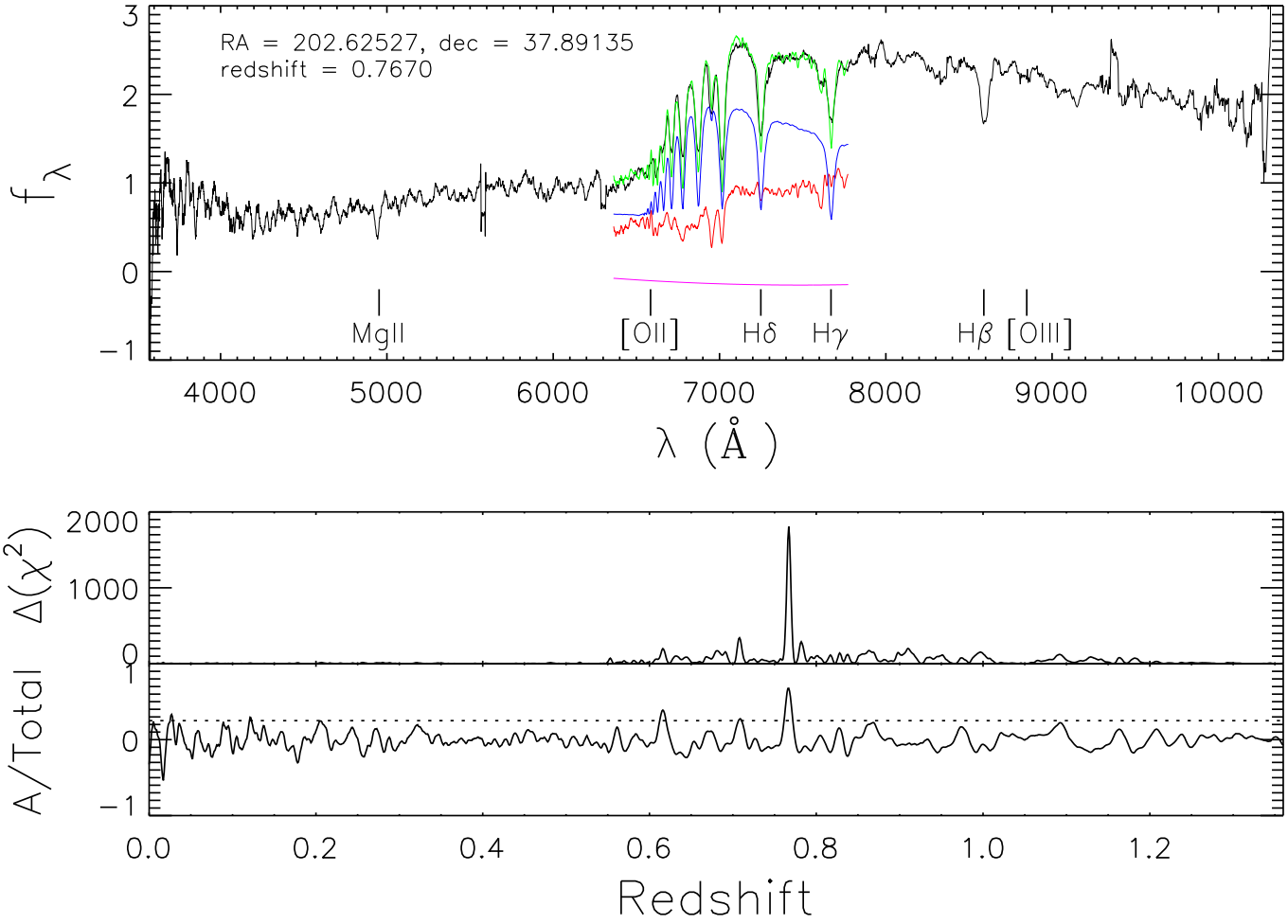

Figure 2. The template fitting procedure is demonstrated in this plot. The object shown is a post-starburst galaxy from BOSS at RA = 202.62527° and DEC = 37.89135° with redshift $z = 0.7670$, observed on plate 3984, fiber 233 and MJD 55333. For this object, the pipeline redshift (Bolton et al. 2012) is accurate. The top panel shows the spectrum of this object, smoothed for increased visibility. Overplotted are the best-fit model (green) with its "K", "A" and polynomial components (red, blue and magenta respectively) at the correct redshift. Positions of several major lines are shown. For this object, there is no emission in [OII]λ3727 as required by our selection criteria, while the Hα line is outside the spectral coverage. The bottom panels show the parameters $\Delta(\chi^2)$ and A/Total of the fit done at all values of assumed redshift within the allowed range. The candidate redshift is where the inclusion of templates in the fit maximally improves the fit, resulting in the peak in $\Delta(\chi^2)$. At this redshift the A/Total ratio is required to be higher than the threshold value of 0.25, represented by the horizontal dotted line, in order to enter the sample. After passing this criterion the fit is visually inspected before the object is included in the final sample.

Line	Bandpass	Blue Sideband	Red Sideband	Reference
[OII]λ3727	3716.30-3738.30Å	3696.30-3716.30Å	3738.30-3758.30Å	Yan et al. (2006)
Hδ	4083.50-4122.25Å	4041.60-4079.75Å	4128.50-4161.00Å	Kauffmann et al. (2003)
Hα	6554.60-6574.60Å	6483.00-6513.00Å	6623.00-6653.00Å	Yan et al. (2006)

Table 1
The definition of the wavelength ranges we used to calculate the equivalent widths for different lines. A line is fitted through both the blue and red sidebands to represent continuum level, which is used for the equivalent width calculation in the central bandpass. The references for the use of these exact values are given in the last column.

Step	SDSS	BOSS
All Spectra	$\sim 1.7 \times 10^6$	$\sim 7.6 \times 10^5$
Program Candidates	8216	23728
Program Candidates ($z > 0.02$)	8216	8485
Visually Inspected	2330	3964

Table 2
The number of spectra considered at each stage of the selection process. The first row is the total number of spectra considered, essentially every spectrum available in the SDSS DR9. The second row is the number of spectra flagged by the selection method to be possible post-starburst galaxy candidates after the fitting process and the application of the cuts on the A/Total ratio and the equivalent widths of the Hδ and [OII]λ3727 lines. The third row is the same as the second row but with the requirement that $z > 0.02$ to remove the contamination from A-stars and white dwarfs. This redshift restriction does not affect SDSS sample since the wavelength coverage does not allow us to probe to such low redshift. The last row is the number of post-starburst galaxies in the final sample after the visual inspection.

lent Width are roughly correlated. This is expected since both are indicators of the strength of the A-star component. Figure 5 shows the distribution of the signal-to-noise ratio in the 4150-4300Å range (median of the per pixel signal-to-noise ratios for all pixels in this wavelength range) of the sample as a function of redshift and rest-frame absolute magnitude in the same wavelength range (denoted by [4200]; for more details on the calculation of this magnitude, see Section 5.2) respectively. Even though we have not made explicit cuts in signal-to-noise ratio, 96% of the objects have signal-to-noise ratio larger than 2, an approximate lower limit to robustly identify post-starburst galaxies (Figure 5). Therefore, the mis-identification due to low signal-to-noise ratio is not a major source of concern for this sample. We quantify the effects of signal-to-noise ratio on selection further below.

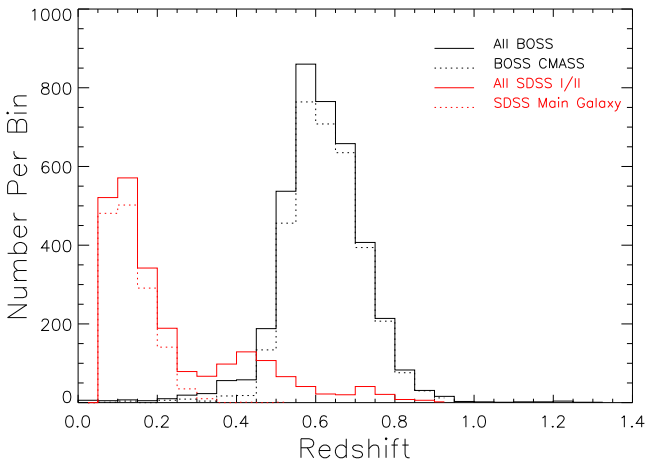

Figure 3. Redshift distributions of post-starburst galaxy samples from both SDSS I/II and BOSS. The solid lines of different colors (red: SDSS I/II, black: BOSS) show the distributions of the entire respective samples, while the dotted lines show the subsamples used to calculate the luminosity function (the Main Galaxy Sample for SDSS, and the CMASS Galaxy Sample for BOSS). Note the tail of objects with redshifts up to $z \sim 1.3$.

4.1. *Coadded Spectra*

The spectra from the sample were coadded to explore post-starburst features at very high signal-to-noise ratio. To do this, the spectra are summed with inverse variance weighting, after bringing all spectra to zero redshift and scaling each by the mean flux density between 4150-4300 Å. The final coadded spectrum, along with the fit of this spectrum into components (Equation 1), are shown in Figure 6. This combined spectrum calculated from the whole sample of several thousand galaxies has very high signal-to-noise ratio and many spectral features are identified with high confidence. A small amount of [OII]λ3727 and Hα in emission can be seen under closer inspection. This is due to emission in individual objects that are small enough to pass the equivalent width cuts.

The coaddition is also done for various different subgroups of galaxies in order to investigate whether the spectra change systematically with properties of the galaxies. The coadded spectra of objects in two redshift bins are in excellent agreement, showing that most of the small-scale features are real. On the other hand, the continuum colors of two redshift bins differ somewhat. As most objects in the low-redshift bin are from SDSS I/II while the high redshift bin is dominated by BOSS objects, this reflects the different selection of the two samples. This selection effect is properly corrected for in the luminosity function analysis in Section 5.

Figure 7 shows the coadded spectra binned by absolute magnitude in the fiducial band at 4200Å. Again, the fine features in the spectra match extremely well between the different bins. The highest luminosity group of objects are significantly bluer longward of 4500Å. There is also a slight difference in continuum level blueward of 3500Å, where the highest-luminosity galaxies have slightly higher continuum level. It is not clear if these differences are due to astrophysical or selection effects. If they are astrophysical, then it means that the more intrinsically luminous objects are more dominated by the A-star population, which has a bluer continuum. On the other hand, these differences could be due to selection effects, because more luminous objects tend to be in the BOSS CMASS Sample, while less luminous objects are likely to be from the SDSS Main Galaxy Sample.

Figure 8 shows the coadded spectra binned by the continuum color below 3500Å, defined as the ratio of the flux density at 2500Å to that at 3100Å, averaged over bandpasses with 200Å width. The composite of the small number of objects with very blue continua (93 out of $\sim$ 3500 which have high enough quality spectra and lie at high enough redshift that this exercise can be carried out) have broad line emission in MgIIλ2803 and NeVλ3426, while the rest of the sample tends to have MgII in absorption. This broad line emission is the distinct signature of post-starburst quasars. Objects with blue continua also tend to show stronger [OII]λ3727 line in emission than the rest of the sample. The difference is small by construction since any object with stronger [OII] emission would not be selected into the sample. This increased [OII] emission can be due to either a small amount of ongoing star formation, or more likely, AGN activity as already suggested by broad MgII emission. This sample can be compared to a bigger sample of SDSS post-starburst quasars presented by Brotherton et al. (2004). Most of those objects have strong enough [OII] emission

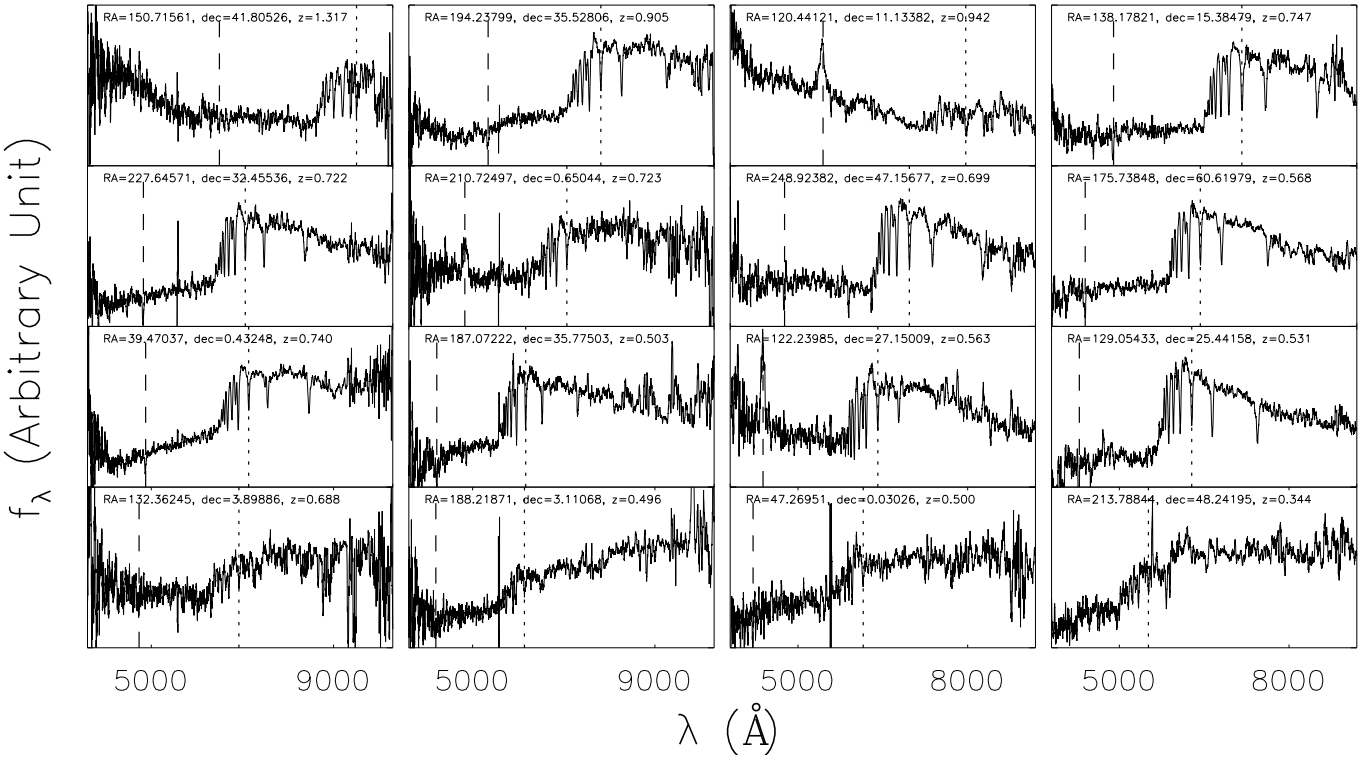

Figure 4. Spectra of a number of objects selected from our final sample. The left half shows objects from the BOSS sample while the right half shows ones from the SDSS I/II sample. The top left corner panel of each side shows the highest-redshift object in each sample. The bottom four panels show objects with noisy spectra to demonstrate the lowest signal-to-noise ratio that could be firmly identified as post-starburst galaxies. The rest of the panels are selected to roughly represent the range of redshift and A/Total ratio spanned by the sample and to also show objects with interesting spectral features, such as blue continuum or MgIIλ2803 line in either absorption and emission. All spectra are smoothed by 10 pixels to show features clearly. Dashed and dotted vertical lines show the position of the MgIIλ2803 and Hδ lines respectively. Many spectra show a residual of the strong sky line at 5577Å.

Survey	RA(°)	DEC(°)	Plate	Fiber	MJD	z	HδEW	[OII]λ3727EW	A/Total	Target Selection	$z = z_{\rm pipe}$
SDSS	120.44121	11.133820	2418	499	53794	0.942	4.80	-1.75	0.32	36700160	False
SDSS	247.71479	47.069620	627	377	52144	0.825	8.06	5.80	0.76	33554433	True
SDSS	35.161773	0.53262315	2637	205	54504	0.646	8.65	-0.29	0.67	32	True
BOSS	165.43852	37.536575	4626	730	55647	1.292	7.43	-0.26	0.54	10995116687360	True
BOSS	233.62838	0.72746109	4010	118	55350	0.941	8.75	-2.00	0.34	3298535538688	True
BOSS	124.34978	34.166264	3758	865	55506	0.823	8.41	0.45	0.69	134	True

Table 3

Example of the full list of post-starburst galaxies presented in this paper to demonstrate the format. The first column indicates whether the object belongs to the SDSS I/II or BOSS subsample. Columns 2-6 are for identification: Right Ascension, Declination and the Plate/Fiber/MJD identification of SDSS spectroscopy. Column 7 is the redshift determined from our selection method. Columns 8-10 are properties used in the selection method, namely the equivalent widths of Hδ and [OII]λ3727 lines, and the A/Total ratio from template fit. Column 11 is the bitmask showing the spectroscopic target selection algorithm. The bitmask can be decoded using information available on the SDSS website `http://www.sdss3.org/dr10/algorithms/bitmask_legacy_target1.php` for SDSS I/II objects, and `http://www.sdss3.org/dr10/algorithms/bitmask_boss_target1.php` for BOSS objects. The last column indicates whether the pipeline redshift (Bolton et al. 2012) agrees with the fit redshift. The objects in this table are unique objects, separated by SDSS I/II and BOSS surveys, and ordered by redshift. The full table is available in `ASCII` format.

that they would be excluded from our sample by our requirement on [OII] equivalent width.

4.2. *Spectroscopic Target Selection*

SDSS and BOSS choose targets for spectroscopic observation based on colors and morphology from the imaging data. Each spectroscopic target is selected by (possibly multiple) selection criteria. Therefore, in order to understand the properties of this sample, it is crucial to understand how each object is selected in the spectroscopic sample into the first place.

Tables 5 and 6 show the breakdown of target selection algorithms by which our post-starburst galaxies are selected, from the SDSS I/II and BOSS sample respectively. In the SDSS I/II sample, the `GALAXY` flag is the dominant target selection algorithm. This corresponds to the Main Galaxy Sample, which is the $r_{\rm petro} < 17.77$ magnitude-limited galaxy sample described in Strauss et al. (2002).

The only other dominant selection flag among the

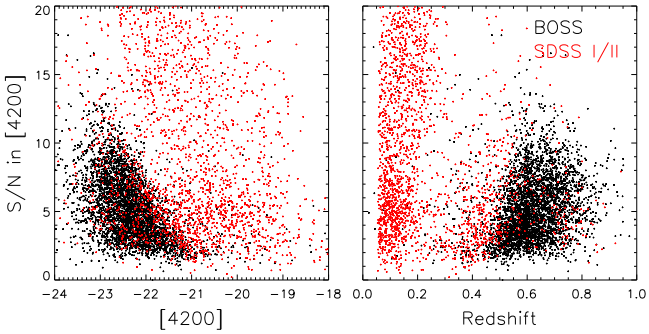

Figure 5. Median signal-to-noise ratio per pixel in the rest-frame wavelength range 4150-4300Å (the "[4200] band") of post-starburst galaxies in our sample, shown as a function of the rest-frame absolute magnitude in the same band (see Section 5.2 for more details) and redshift. The red and black points represent objects from SDSS-I/II and SDSS-III BOSS samples respectively. There are very few objects with S/N< 2, which is an empirical lower limit for robustly identifying post-starburst galaxies.

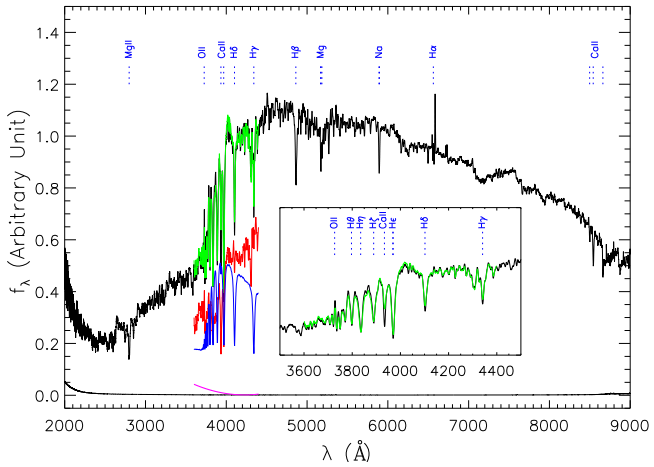

Figure 6. The coadded spectrum of the post-starburst galaxy sample from both SDSS and BOSS, with line features identified. The black solid line at the bottom of the plot shows the per-pixel error of the spectrum. The errors are very close to zero over most of the spectral range, indicative of very high signal-to-noise ratio. The inset shows the spectrum in the 3600-4400 Å region, which is used for template fitting, in more detail. The green curve shows the model fit to this coadded spectrum, with the "K", "A" and Polynomial components of the model shown in red, blue and magenta respectively. Note that the polynomial component is small in this coadded spectrum, as it is for most individual objects. It should be noted that at the short and long wavelength ends ($\lambda < 3000$Å and $\lambda > 8000$Å), the coadded spectrum is derived from only a small number of objects and thus may not be very reliable.

SDSS I/II sample is `QSO_HIZ`, which is designed for the high-redshift quasars. A significant number of objects are selected through this flag because they appear unresolved, as required by the high-redshift quasar selection criteria, and the broadband color of the Balmer break at redshift less than unity resembles the Lyman break at redshift $z \sim 3-4$ (Fan et al. 1998).

For the BOSS sample, the dominant selection flags are all related to the CMASS program, which is the "Constant Stellar Mass" sample of luminous galaxies with redshift $0.4 < z < 0.7$ designed to measure Baryon Acoustic Oscillations (Anderson et al. 2012; Dawson et al. 2013). The most important of these flags is the `GAL_CMASS` flag.

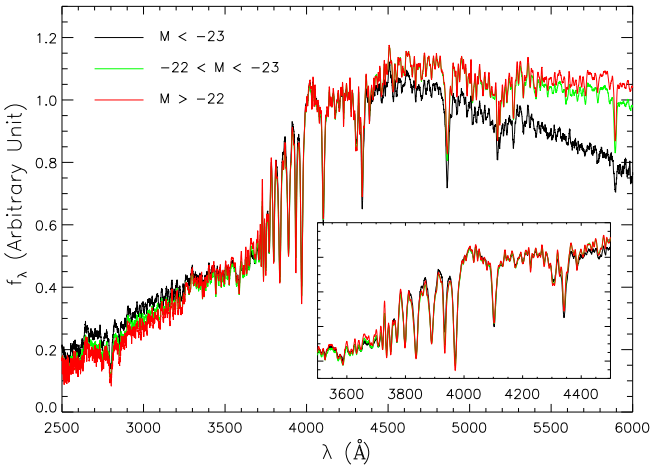

Figure 7. The coadded spectrum of the post-starburst galaxy sample binned by absolute magnitude in our fiducial [4200] band. The black, green and red lines are the most, intermediate and least luminous groups respectively. The small spectral features match in detail in these independent coadds, demonstrating that they are real. The differences in overall SED shapes may be due to either the intrinsic properties of the stellar populations, or selection effects.

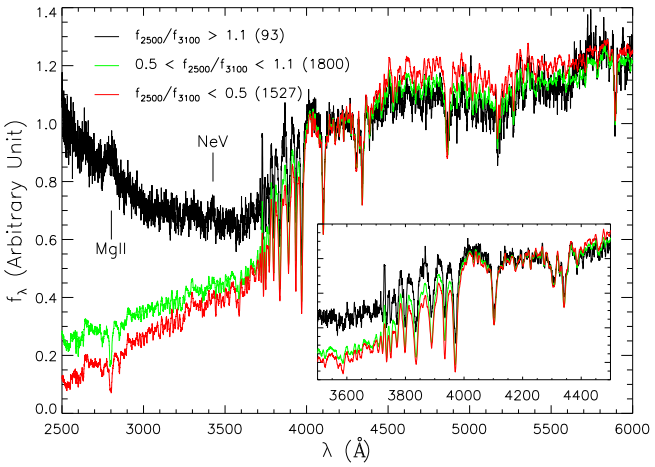

Figure 8. The coadded spectra of the post-starburst galaxy sample binned by the continuum color below 3500Å, defined as the ratio of flux density at 2500Å to that at 3100Å, averaged over bandpasses with 200Å width. The numbers of objects in each bin are shown in parentheses. The most dramatic feature, in addition to the slight difference in continuum color at the red side of 4000Å break, is that the composite spectrum of objects with extremely blue continuum shows broad line MgIIλ2803 emission, while the rest of the sample shows it in absorption. Additionally, NeVλ3426 in emission can be seen in this population. That is, these are post-starburst quasars, showing both AGN features (blue continuum, broad line emission) and post-starburst spectral features.

The flags `GAL_CMASS_COMM` and `GAL_CMASS_ALL` were used in the early part of the survey to tune the CMASS selection criteria, and are therefore more inclusive but less complete. When we calculate the luminosity function for the CMASS galaxies (Section 5), we limit our sample to the objects selected by the `GAL_CMASS` flag only. It should also be noted that very few objects in our sample are part of the other major BOSS galaxy sample, the LOWZ sample.

Sample	Number of Objects
BOSS entire sample	3964
$z_{\rm fit} = z_1$	3900 = 98.38%
SDSS entire sample	2330
$z_{\rm fit} = z_1$	2194 = 94.16%
SDSS z_2 exists	2223
$z_{\rm fit} = z_1$	2106 = 94.74%
$z_{\rm fit} = z_2$	2153 = 96.85%
$z_{\rm fit} = z_1$ but $z_{\rm fit} \neq z_2$	47 = 2.11%
$z_{\rm fit} = z_2$ but $z_{\rm fit} \neq z_1$	94 = 4.23%
$z_{\rm fit} = z_1 = z_2$	2059 = 92.62%
$z_{\rm fit} \neq z_1 \neq z_2$	23 = 1.03%
SDSS z_2 does not exist	107
$z_{\rm fit} = z_1$	88 = 82.24%

Table 4
The breakdown of our post-starburst galaxy sample in terms of whether the redshifts determined by the spectroscopic pipelines agree with those from our fitting procedure. In this table, z_1 indicates the `idlspec2d` redshift from the main spectroscopic pipeline (Bolton et al. 2012) which is available for both samples, while z_2 is the `spectro1d` redshift (SubbaRao et al. 2002), which is available for most of the SDSS I/II sample, but not for BOSS.

4.3. *Comparison to the Pipeline Redshifts*

We mentioned in Section 3.2.2 that some of the high-redshift post-starburst galaxies have incorrect pipeline redshifts. We now discuss this issue in more detail.

Table 4 summarizes the comparison between pipeline redshifts and our measured redshifts for our post-starburst galaxy sample. The sample from SDSS I/II is broken down by availability of the second pipeline redshift. For this sample, the main spectroscopic pipeline (`idlspec2d`) redshift (Bolton et al. 2012) and the `spectro1d` redshift (SubbaRao et al. 2002) are each incorrect for 4-6% of our galaxies. The BOSS post-starburst sample has better redshift determination; it is incorrect for only about 2% of our objects. The main reason the pipeline redshifts are incorrect is the lack of post-starburst spectral templates in the spectroscopic pipeline. This was improved in the BOSS sample, resulting in better redshift determination. Other reasons for incorrect redshift determinations are artifacts in the data that significantly change the shape of the continuum, such as bad CCD columns or light leakage from bright object in adjacent fibers, or simply too low signal-to-noise ratio. In most (but not every) of these cases, the `ZWARNING` flag is set by the pipeline to indicate low confidence in the redshift.

Two objects with discrepant redshifts are particularly interesting: they are actually pairs of objects along the same line of sight at different redshifts. In these cases, our post-starburst galaxy selection method identifies one object of the pair, while the SDSS spectroscopic pipeline correctly identifies another. These systems are shown in Figure 9 with various line features identified. The first system is a post-starburst galaxy at redshift $z = 0.861$ with a star-forming galaxy at redshift $z = 0.3532$. The second system is a post-starburst galaxy at redshift $z = 0.738$ and a quasar at redshift $z = 1.8039$. These objects may be interesting for follow-up observations to study strong gravitational lensing or absorption spectroscopy of outflows, for example.

4.4. *Hα Equivalent Width*

Selection Criteria	Number
Total	2330
Main Galaxy Sample	1462
All Galaxy	1879
Luminous Red Galaxy	140
Quasar	406
ROSAT	32
Stellar	30
Serendipitous	66

Table 5
The breakdown of our post-starburst galaxies sample from the SDSS I/II sample in terms of the spectroscopic target selection algorithms by which they are selected. The second row is the magnitude-limited main galaxy sample that we use in our luminosity function analysis. The other rows show the number of objects selected by various broad groups of selection algorithms. Note that a galaxy can be selected by more than one algorithm.

Selection Criteria	Number
Total	3964
CMASS Sample	3475
Galaxy	3810
Quasar	72
Spectral Template	5

Table 6
The breakdown of our post-starburst galaxies sample from the BOSS sample in terms of the spectroscopic target selection algorithms by which they are selected. The second row is the CMASS Sample with well-defined selection that we use in our luminosity function analysis. The other rows show the number of objects selected by various broad groups of selection algorithms. Note that a galaxy can be selected by more than one algorithm.

In our selection of this sample, we have neglected the Hα line and only considered two lines (Hδ in absorption and lack of [OII]λ3727 in emission) since most objects we select for are at high enough redshift that the Hα line is redshifted out of the wavelength coverage of the spectra. In order to compare this to other works and understand any biases the lack of selection in Hα might introduce, we need to quantify how strong Hα is in these objects. This exercise is important for two reasons. The first is because the Hα line is commonly used as an indicator of star formation rate in most previous studies of E+A galaxies at low redshift. The second reason is that AGN are also known to produce Hα emission, and therefore can introduce selection biases. We address this concern with two different approaches.

The first one is to use our sample (mainly from SDSS-I/II) at low enough redshift that Hα lies in the SDSS spectra. Figure 10 shows the distribution of Hα equivalent width as a function of the absolute magnitude in the rest-frame [5000] band (this band is used in Section 5.2 for our luminosity function calculation) for the 1766 SDSS-I/II post-starburst galaxies at $z < 0.33$. Among these objects only 968 (54%) have HαEW > -3.0Å, the selection criterion adopted by Goto (2007). This means that nearly half of the sample at low redshift would be dropped as star forming if Hα were taken into consideration, a rate consistent with what Goto (2007) found. However, if one limits the consideration to only the intrinsically luminous galaxies, the contamination is minimal. This can be seen from the subsample with absolute [5000] magnitude brighter than -22.5. Out of 154 ob-

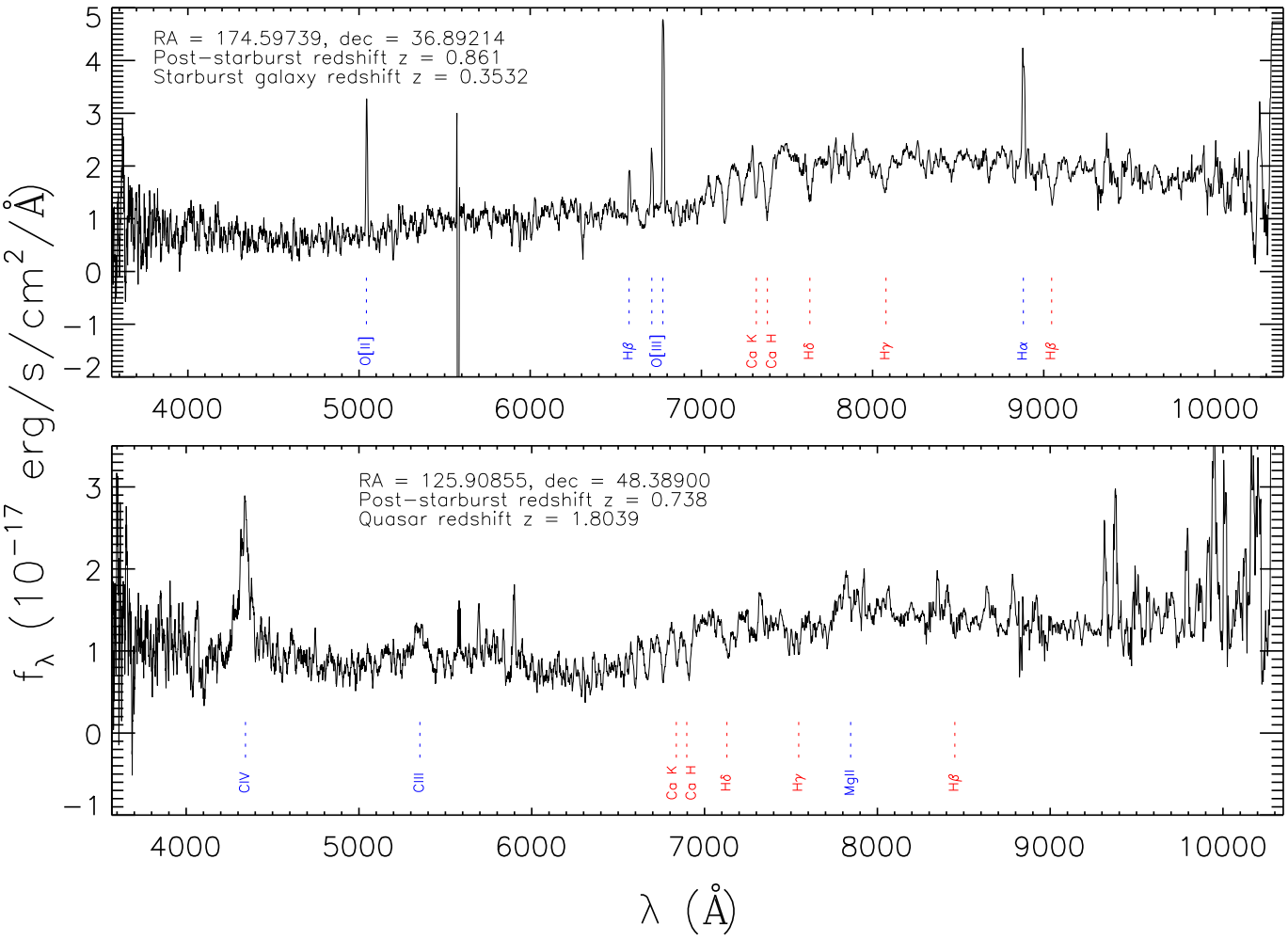

Figure 9. Two interesting objects that were discovered serendipitously because the pipeline redshifts and the fit redshifts disagree. They are actually pairs of objects along the same line of sight at different redshifts. The top panel shows a post-starburst galaxy at redshift $z = 0.861$ with a star-forming galaxy at redshift $z = 0.3532$. The bottom panel is a post-starburst galaxy at redshift $z = 0.738$ with a quasar at redshift $z = 1.8039$. The spectral features belonging to the post-starburst galaxies in each plot are indicated in red, while the ones belonging to the superposed objects are indicated in blue. These spectra are smoothed with a 10 pixel boxcar average to show the features clearly.

jects in this subsample, only 11 objects (7%) have HαEW > -3.0Å. Since most of our targets at high redshifts selected from BOSS are more luminous than $M \sim -22.5$ in the same band, and under the assumption that the post-starburst galaxies of the same intrinsic brightness have the same properties across cosmic time, we can extrapolate from this bright, low-redshift sample to conclude that our high-redshift sample from BOSS is minimally contaminated by our lack of Hα information.

At the high-redshift end, we conducted follow-up near-IR spectroscopic observations on a small number of objects to observe Hα directly. We observed 10 objects at $z \sim 0.8$ with the TripleSpec instrument (Wilson et al. 2004) on the ARC 3.5m telescope at the Apache Point Observatory. The follow-up observations took place between November 2011 and November 2013, with details shown in Table 7. The targets were selected such that the Hα line is expected to be in a region clear of telluric absorption, and to be as bright as possible for maximum signal-to-noise ratio. The exposure times were between 40 minutes and 104 minutes per object. The spectra were reduced using the publicly available software TripleSpecTool, which is a modified version of Spextool developed by Cushing et al. (2004). The software uses the telluric correction algorithm developed by Vacca et al. (2003).

The objects are clearly detected in the continuum, but are too faint to have good enough signal-to-noise ratio to detect the Hα line either in absorption or emission. The composite spectrum of these objects at rest-frame Hα wavelength is shown in Figure 11 and the equivalent width of Hα calculated from this composite using a simple estimate is HαEW $\approx -4 \pm 6$ Å, consistent with zero. This lack of any clear detection is consistent with our low-redshift finding that luminous post-starburst galaxies selected only from Hδ and [OII]λ3727 are minimally contaminated by objects with large Hα emission. The [NII]λ6584 emission is detected in this composite spectrum with reasonable confidence. At face value, high [NII] to Hα ratio suggests that the spectrum is dominated by an AGN. However, it is also possible that the Hα absorption from the post-starburst spectrum is offset by Hα emission from a starburst or AGN component re-

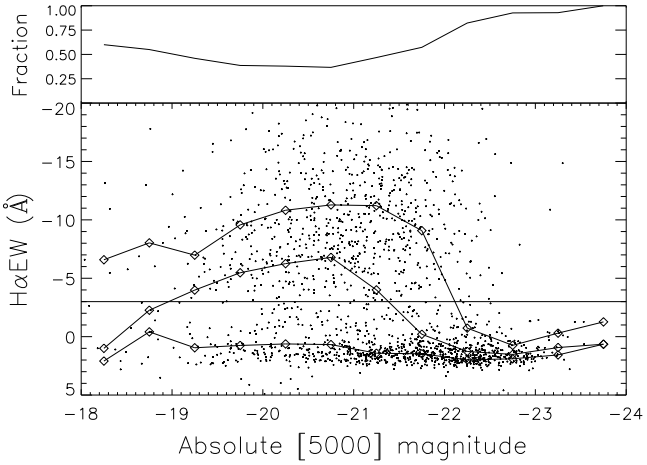

Figure 10. Rest-frame Hα Equivalent Width against the absolute magnitude in the [5000] band for post-starburst galaxies from SDSS I/II sample with redshift $z < 0.33$, selected irrespective of their Hα properties. In the sign convention used here, positive values of Equivalent Width correspond to absorption. The horizontal line indicates the selection criteria HαEW > -3.0Å used by Goto (2007). The three lines with square symbols are the 25, 50 and 75 percentiles of the objects in each half-magnitude bin respectively. The top panel shows the fraction of objects that pass the Goto (2007) selection criteria in each bin.

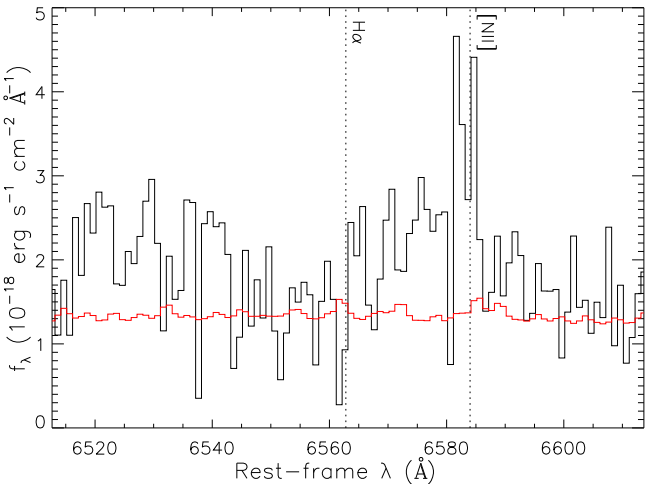

Figure 11. The composite spectrum around the wavelength of Hα of 10 post-starburst galaxies that were observed by the TripleSpec instrument at the APO 3.5m telescope. The noise level is shown by the red line. The expected positions of Hα and [NII]λ6584 are shown by the dotted vertical lines. The continuum of these objects is clearly detected, but the signal-to-noise ratio is too low for Hα to be seen either in emission or absorption. The [NII] emission is detected with reasonable confidence.

sulting in a non-detection in this line (e.g., Rubin & Ford (1986)).

4.5. *Potential Biases in Selection*

In this section, we discuss potential selection biases in our post-starburst galaxy sample. It is common to use the strength of [OII]λ3727 and Hα emission to measure the star formation rate, in order to make cuts in these quantities and select objects with little or no ongoing star formation. However, AGN also produce emission in both lines. Therefore, when AGN are present, it is inevitable that biases are introduced when selecting a sample using these lines. In this work, we select post-starburst galaxies based on the Hδ and [OII] lines; we discussed the bias due to not considering the Hα line above in Section 4.4.

Objects that have intrinsically post-starburst stellar populations, but have significant [OII] emission due to AGN/LINERs (Yan et al. 2006) will be removed from the sample by the [OII] equivalent width cut. The degree of this bias is harder to quantify, since it can be difficult to distinguish galaxies that have post-starburst population with AGN and those with ongoing star formation, at least at the resolution and signal-to-noise ratio of SDSS spectra.

We note that the sample of post-starburst galaxies presented in this work is defined in a practical way, based on the equivalent widths of two lines. Therefore, it does not correspond exactly to the galaxy population whose stellar populations are intrinsically post-starburst, regardless of the presence of an AGN. In the luminosity function calculation in the next section, we attempt to carefully correct for these biases and check for self-consistency when possible.

Another source of bias is the incompleteness in the SDSS spectroscopic sample itself. About 5% of objects targeted for spectroscopy do not have usable spectroscopic data in the end. This effect is largely dominated by fiber collision, with a small fraction due to low signal-to-noise ratio that prevents redshift measurements. This incompleteness is a weak function of redshift and magnitude, since faint objects at high redshift tend to have lower signal-to-noise ratio. All luminosity functions derived in this paper are divided by 0.95 to correct for this incompleteness.

Date observed	RA	DEC	Redshift	Exposure time
16 Nov 2011	01:36:11.85	+00:30:04.39	0.7886	48 mins
16 Nov 2011	02:49:56.15	-00:59:05.65	0.8270	56 mins
02 Jun 2012	16:46:24.77	+28:23:12.56	0.8560	64 mins
12 Jun 2012	12:32:54.27	+00:22:43.12	0.8499	40 mins
05 Sep 2013	21:15:33.74	+00:22:47.93	0.8338	84 mins
05 Sep 2013	01:13:33.06	+02:50:26.32	0.8980	92 mins
05 Sep 2013	02:29:24.93	-03:36:33.60	0.8520	56 mins
19 Nov 2013	21:20:56.53	+00:01:13.24	0.8381	76 mins
19 Nov 2013	23:51:41.07	+03:05:42.60	0.8570	60 mins
19 Nov 2013	02:08:51.52	+05:52:28.04	0.8269	104 mins

Table 7
Details of follow-up observations of high-redshift post-starburst galaxies using the TripleSpec instrument at the Apache Point Observatory (APO) 3.5m telescope.

5. LUMINOSITY FUNCTION

5.1. *Synthetic Spectrophotometry*

In order to calculate the luminosity function of post-starburst galaxies, one needs the selection function of the sample, i.e., the probability of selecting a given galaxy as a function of redshift, given its luminosity and spectral shape. Given that we already have well-calibrated spectra for every object in our sample, we can synthesize the photometry of an object at any redshift by shifting the spectrum and scaling the brightness to that redshift, reconstructing the magnitudes and tracing through the selection criteria. This process automatically incorporates the k-correction and the dimming of objects with redshift (the inverse square law). We also quantified and

corrected for the incompleteness due to changes in signal-to-noise ratio as a function of assumed redshift. The details of these processes are as follows.

We calculate the synthesized magnitude in the g, r and i bands that a given galaxy would have, on a grid of redshift ranging from $z_{\rm min}$ to $z_{\rm max}$ (determined as the redshift range where the 3600-4400Å region would be inside the spectral coverage, as used in the post-starburst selection method discussed earlier), with a grid spacing of $\Delta z = 0.001$. For each value on this redshift grid, the spectrum of the object is shifted, then integrated over each required band to find the average flux density over the band.

For the vast majority of assumed redshifts, the g, r and i filters fall within the observed spectral coverage. If not, we extrapolate the spectrum using the best-fit model from the spectroscopic pipeline (Bolton et al. 2012). In rare cases when even the model does not have the required spectral coverage, the magnitude is calculated from linear extrapolation from nearby redshift values.

This average flux density is then scaled to take into account the inverse square law by the multiplicative factor $\left(\frac{1+z_{\rm obs}}{1+z_{\rm ass}}\right)\left(\frac{D_L(z_{\rm obs})}{D_L(z_{\rm ass})}\right)^2$, where $z_{\rm obs}$ is the observed redshift of the object, $z_{\rm ass}$ is the assumed redshift at this particular gridpoint and $D_L(z)$ is the cosmological luminosity distance evaluated at these redshifts. The relationship between $D_L(z)$ and z is from the standard ΛCDM cosmology with $\Omega_M = 0.3$, $\Omega_\Lambda = 0.7$ and $H_0 = 70\,{\rm kms^{-1}Mpc^{-1}}$. This scaled average flux density is then turned into AB magnitude, with the Schlegel et al. (1998) galactic extinction of the object in the same band corrected for. This extinction correction assumes the standard total-to-selective extinction ratio $R_V = 3.1$. We call this class of magnitude derived from the spectrum the "Spectro" magnitude, as we described in Section 2.2.

Next, these Spectro magnitudes in the g, r and i bands are converted into various other kinds of magnitudes that are used in the spectroscopic selection algorithms (Section 4.2), namely the Model, cModel, Petrosian and Fiber magnitudes (Section 2.2). This conversion is done for each kind of magnitude by applying the difference between the Spectro magnitude and that kind of magnitude at the observed redshift. This single-valued conversion is justified because at the redshifts relevant for the CMASS Sample, the angular diameter distance is a slowly changing function of redshift. The appearances of the images observed, except for brightness, are relatively constant, therefore the difference between families of magnitudes that arise from different ways to process this image should not change very much with redshift. Once this process is done, we have determined various magnitudes in the g, r and i bands as a function of assumed redshift. At the lower redshift range relevant to SDSS I/II sample, the justification that the angular-diameter distance is a slowly changing function of redshift is no longer true, and the use of the single-valued correction might be less justified. However, we still expect that it is largely valid given the small redshift range ($\Delta z \sim 0.2$) involved.

5.2. *Magnitude and Color in Fiducial Bands*

In order to compare intrinsic luminosities of objects over a range of redshift, the magnitudes in the observed bands are not sufficient, since they sample different parts of the spectrum at different redshifts, and thus need to be k-corrected. For this purpose, we calculate the absolute AB magnitude from the spectra in two fiducial top-hat bands fixed in rest-frame wavelength from the spectra for all our objects from the SDSS I/II and BOSS samples. The first is the fiducial band we have introduced before; it lies between 4150Å and 4300Å, sampling the continuum between the Hγ and Hδ lines. The other band is between 4950Å and 5100Å. As introduced earlier, we will refer to these bands as the [4200] and [5000] bands respectively. These two wavelength ranges roughly represent the wavelength coverage for the r and i bands at redshift $z \sim 0.5$, and lie in continuum regions without strong absorption lines. The magnitude in the [4200] band is available for every object in our sample, because our selection process guarantees that this rest-frame wavelength is covered in the spectrum. The same is not true for the [5000] band, since it is shifted outside the spectral coverage for redshift greater than around unity. However, galaxies in subsamples with homogeneous selection that will be used to calculate the luminosity function (the SDSS Main Galaxy Sample and the BOSS CMASS Sample) do not extend to such high redshift, so this is not an issue.

For each band, the averaged flux density $\bar{f}_\lambda$ in the band is calculated from the spectrum, then scaled to 10 parsec by the factor $(1+z)\left(\frac{D_L(z)}{10{\rm pc}}\right)^2$ for the calculation of absolute magnitude in the AB system. This Spectro magnitude is then converted to cModel magnitude using the observed difference between cModel and Spectro magnitude from the SDSS bands, and interpolated to the wavelength where the fiducial band under consideration lies at the observed redshift. Galactic extinction is corrected in the same manner, using the extinction in SDSS bands interpolated to the appropriate wavelength where the fiducial band lies.

Figure 12 shows the scatter plot between this absolute magnitude in the [5000] band and redshift of the objects, together with the respective approximate selection limit, in both the SDSS I/II and BOSS samples. The selection limits are calculated from the coadded spectrum of the sample, showing the absolute magnitude corresponding to when the spectrum is scaled to match the selection limits of the respective surveys. Even before calculating the luminosity function properly, this plot gives a number of qualitative insights into the luminosity function of these two subsamples of post-starburst galaxies.

First of all, there is a dramatic difference between the luminosity ranges over which the post-starburst galaxies lie at low and high redshift, as seen by comparing the SDSS Main Galaxy Sample and the BOSS CMASS Sample. The low-redshift sample ranges from -19 to -23 magnitude, while the high-redshift sample ranges from -22 to -24 magnitude and even brighter. It is noteworthy that there are very few low-redshift post-starburst galaxies brighter than -23 magnitude, even though if luminous galaxies existed at low redshift they would certainly have been observed and selected into the sample, although this could be due to small volume sampled. From this, we expect that the number density of lumi-

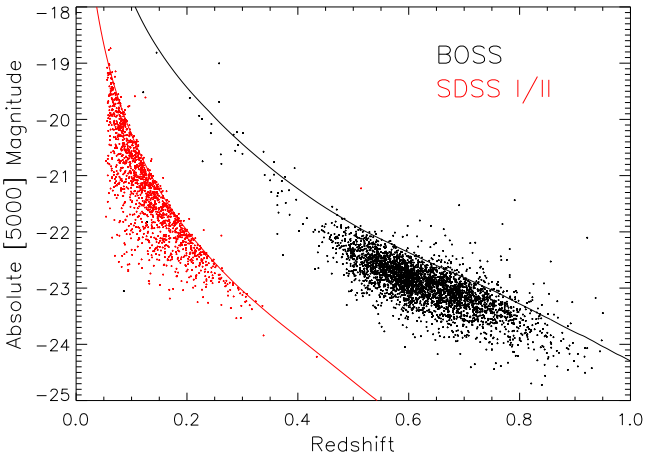

Figure 12. Absolute magnitude in the fiducial band [5000] against redshift for our post-starburst galaxies from both the SDSS Main Galaxy Sample (red) and the BOSS CMASS Sample (black). The solid lines show the corresponding selection limits of each sample for the mean SED ($r_{\rm petro} < 17.77$ for SDSS and $i_{\rm cmodel} < 19.9$ for BOSS). These lines are calculated from the coadded spectrum of the sample, such that they show the absolute magnitude in the [5000] band when the spectrum is scaled to match the selection limits of the respective surveys at each value of redshift. Note that these selection lines are not hard cuts, and the fact that some objects lie above the lines is due to the variation in the SEDs from the coadded spectrum.

nous post-starburst galaxies at high redshift is significantly higher than that at low redshift; this is a downsizing trend.

This trend can also be seen within the low and high redshift samples separately. For example, at redshift $z \sim 0.1$ there are fewer galaxies at -23 magnitude than at redshift $z \sim 0.2$, and also at redshift $z \sim 0.55$ there are fewer galaxies at -23.5 magnitude than at $z \sim 0.75$. Therefore we expect just from this plot (Figure 12) that the luminosity functions of post-starburst galaxies as a function of redshift should show a downsizing trend. In other words, luminous post-starburst galaxies are more abundant at higher redshift. Quantifying this requires taking into account the selection effects and the fact that the effective volume of the survey is larger at higher redshift, as we will do in what follows.

It is also noteworthy that the post-starburst galaxies selected from the BOSS CMASS Sample have systematically higher redshift than the overall CMASS Galaxy Sample; the median redshift of CMASS post-starburst galaxies is $z \sim 0.63$, while that of the whole CMASS Sample is $z \sim 0.57$. This is likely due to systematic differences in the SEDs of post-starburst galaxies and the generic massive early-type galaxies which are the main target of CMASS color selection.

5.3. *SDSS Main Galaxy Sample*

The SDSS Main Galaxy Sample is simply magnitude-limited at $r_{\rm petro} < 17.77$. For each of our post-starburst galaxies from the SDSS Main Galaxy Sample, we use the Petrosian magnitude as a function of assumed redshift calculated from the spectrum (see Section 5.1) to determine the redshift range over which this galaxy would be selected into the SDSS spectroscopic sample. Because our spectra extend to 3800 Å, we can only select post-starburst galaxies at $z > 0.02$.

We also calculate the effects of finite signal-to-noise ratio on our selection function for each galaxy using Monte-Carlo simulations. This completeness fraction, $\mathcal{C}(z)$, is defined as the fraction of realizations, out of 1000 total realizations at each assumed redshift, that a specific spectrum is selected as a post-starburst galaxy by our selection criteria (A/Total>0.25, HδEW > 4.0Å and [OII]λ3727EW > -2.5Å) after adding random noise at the appropriate level. In this calculation, we use the best-fit template between rest-frame 3600-4400Å range, scaled for cosmological dimming, as the "noiseless model", while the noise is taken from the sky background at the wavelength range corresponding to rest-frame 3600-4400Å at that redshift. This noise model is appropriate because at these magnitudes, the sky noise completely dominates over the photon noise from the object itself. For majority of objects, the completeness fraction $\mathcal{C}(z)$ remains near unity over the relevant redshift ranges. The cosmological volume $V_{\rm max}$, within which the object can be observed, is then calculated as

$$V_{\rm max} = \frac{\Omega}{4\pi} \int_{z_{\rm min}}^{z_{\rm max}} \mathcal{C}(z)\, dV, \tag{2}$$

where Ω corresponds to the solid angle of the SDSS survey up to DR7, 8032 deg^2. In cases that we calculate the luminosity function in a redshift bin, this volume $V_{\rm max}$ is further restricted to be only the volume that overlaps with that redshift bin.

The luminosity function of post-starburst galaxies from the SDSS Main Galaxy Sample is calculated using the standard $1/V_{\rm max}$ method. The sample is split into two redshift bins at redshift cut $z = 0.12$, resulting in roughly the same number of objects in each bin. We impose an upper limit on redshift for the $z > 0.12$ bin at $z = 0.35$, which essentially contains all the post-starburst galaxies selected from the Main Galaxy Sample. The luminosity functions are then divided by a factor of two at magnitudes fainter than $M \sim -22$ to statistically take into account the contamination from objects with strong Hα emission (see Section 4.4 and Figure 10). It is worth noting that this correction may overcorrect for the contamination at faint magnitudes, since some objects might have intrinsically post-starburst stellar populations, but with AGN causing their removal from the sample. The resulting luminosity functions for galaxies in this sample for both redshift bins (along with that of the CMASS Sample, see next section) are shown in Figure 19.

5.4. *BOSS CMASS Sample*

For the BOSS CMASS Sample, the spectroscopic target selection criteria are designed to select an approximately volume-limited sample of galaxies in the range $0.4 < z < 0.7$ to measure Baryon Acoustic Oscillations in their clustering (Anderson et al. 2012; Reid et al. 2016). CMASS stands for "Constant Mass", and the following criteria are designed to be crude cuts in both photometric redshift and stellar mass, isolating objects with mass $> 10^{11} M_{\odot}$. These selection criteria are

$$17.5 < i_{\rm cmod} < 19.9 \tag{3}$$

$$r_{\rm mod} - i_{\rm mod} < 2.0 \tag{4}$$

$$d_\perp = r_{\rm mod} - i_{\rm mod} - (g_{\rm mod} - r_{\rm mod})/8.0 > 0.55 \quad (5)$$

$$i_{\rm fib2} < 21.5 \quad (6)$$

$$i_{\rm cmod} < 19.86 + 1.6(d_\perp - 0.8), \quad (7)$$

with two additional star-galaxy separation cuts

$$i_{\rm psf} - i_{\rm mod} > 0.2 + 0.2(20.0 - i_{\rm mod}) \quad (8)$$

$$z_{\rm psf} - z_{\rm mod} > 9.125 - 0.46 z_{\rm mod}. \quad (9)$$

The star-galaxy separation cuts are used to select extended sources by comparing the PSF magnitudes to the model magnitudes. Due to the slowly varying nature of the angular diameter distance with redshift for the relevant redshift range of this sample, we expect that any object that satisfies the star-galaxy separation at its observed redshift and enters the CMASS Sample in the first place would also satisfy these conditions over the entire redshift range. Therefore we do not consider these cuts from our calculation of the selection function.

However, some post-starburst galaxies may be unresolved, and thus will not be targeted at all by CMASS. Indeed, ∼2% of our objects are targeted as unresolved quasar candidates, but this fraction is small enough not to alter the luminosity function results significantly. We therefore calculate the luminosity function only from objects selected as CMASS galaxies.

The distribution of objects in our sample in the various color-magnitude spaces probed by these criteria are shown in Figure 13. It can be seen that the three most restrictive conditions for our samples are $i_{\rm cmod} < 19.9$, $d_\perp > 0.55$ and $i_{\rm cmod} < 19.86 + 1.6(d_\perp - 0.8)$.

Another potential selection bias that should be noted is the fact that our selection method is designed to target relatively older post-starburst galaxies (older than ∼50 Myr, the lifetime of a B3 star, which is the least massive star that produces [OII] emission in the surrounding HII region), leading to incompleteness in the blue end of the sample (as discussed earlier in Section 3.2.4). For the BOSS CMASS subsample, which is designed to target red, luminous galaxies through this color selection, this effect might add extra incompleteness to the blue, faint end of the sample.

We use the prediction of brightness as a function of assumed redshift based on the observed SED (see Section 5.1) to find the redshift range over which all criteria are satisfied, as demonstrated in Figure 14. This range corresponds to the redshifts that the object would still be selected into the spectroscopic sample and subsequently our post-starburst galaxy sample. We also take into account the effect of finite signal-to-noise ratio by using Monte-Carlo simulations as described in Section 5.3, by adding appropriate random noise based on the sky background and measuring the A/Total ratio and Hδ and [OII] equivalent widths for each noise realization, resulting in the completeness fraction $\mathcal{C}(z)$. The behavior of $\mathcal{C}(z)$ as a function of assumed redshift, which is more complete at lower redshift and starts to degrade at higher redshift due to lower signal-to-noise ratio, is typical of the objects in the sample. The cosmological volume a galaxy can be observed $V_{\rm max}$ is calculated using Equation 2, with the solid angle corresponding to

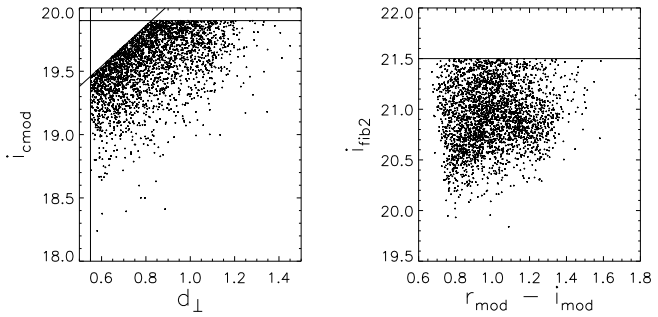

Figure 13. Our post-starburst galaxies from the BOSS CMASS Sample shown against the CMASS selection criteria. The left panel shows the distribution of the cModel i-band magnitude against the color $d_\perp$. The lines shown are the relevant selection criteria $i_{\rm cmod} < 19.86 + 1.6(d_\perp - 0.8)$, $i_{\rm cmod} < 19.9$ and $d_\perp > 0.55$, with $i_{\rm cmod} > 17.5$ off the scale. The right panel shows the Fiber2 i-band magnitude against the $r - i$ color. The selection line shown is $i_{\rm fib2} < 21.5$, with $r_{\rm mod} - i_{\rm mod} < 2$ off the scale. All colors and magnitudes plotted here are corrected for the Schlegel et al. (1998) galactic extinction.

SDSS DR9 area of 3275 deg^2. For a redshift bin, the volume $V_{\rm max}$ is further restricted to be only the overlapping volume with that redshift bin.

Even after the volume $V_{\rm max}$ is known, simply summing the inverse of this volume in bins of magnitudes is not sufficient to get an unbiased luminosity function. This is due to a consequence of the CMASS color selection that not all SEDs are selected at all luminosities. We now describe the process we adopt to correct for this effect.

Figure 13 shows the selection of the CMASS galaxies in observed quantities, but in order to obtain a physically meaningful measure of the luminosity function, we need to work in terms of the intrinsic, rest-frame properties of the galaxies. We measure these intrinsic quantities by using the two fiducial bands at 4200Å and 5000Å that we introduced earlier. Note again that these two bands lie at the approximate wavelengths of the r and i bands at redshift $z = 0.5$, and the quantity $d_\perp$ is dominated by r and i. Therefore we expect that the selection criteria in terms of $i_{\rm cmod}$ and $d_\perp$ should translate roughly to cuts in the [5000] and [4200] − [5000] plane. Figure 15 shows this plane; galaxies are indeed roughly bounded by the cuts shown. We see that the color distribution of galaxies in this space becomes increasingly restricted fainter than $M = -23.0$, which would introduce biases in the luminosity function if not corrected for. In this parameter space, we define the selection lines to be $-24.1 < [5000] < -22.2$, $0.2 < [4200] - [5000] < 1.2$ and $[5000] < -23.3 + 1.8([4200] - [5000])$. These selection lines are drawn arbitrarily to have a similar form to the CMASS selection in observed quantities, with values such that they roughly represent the distribution in Figure 15. In order to have a uniformly selected sample, we do not include any galaxy that falls outside this range in our luminosity function analysis. Figure 16 shows the distribution in this parameter space but separated into different redshift bins. For the BOSS CMASS Sample, populations at different redshifts fall into different region of this parameter space, but remain bound by the fiducial selection cuts.

This correction works under the assumption that the distribution of number density of galaxies is a separable function of magnitude and color. Thus knowing the

Survey	Redshift Range	Total Number	After Fiducial Selection Cuts	Median Redshift
SDSS Main Galaxy	All Redshifts	1462	1462	0.124
SDSS Main Galaxy	$0.02 < z < 0.12$	696	696	0.091
SDSS Main Galaxy	$0.12 < z < 0.35$	766	766	0.160
BOSS CMASS Galaxy	All Redshifts	3475	2867	0.624
BOSS CMASS Galaxy	$0.45 < z < 0.55$	649	437	0.521
BOSS CMASS Galaxy	$0.55 < z < 0.65$	1462	1331	0.599
BOSS CMASS Galaxy	$0.65 < z < 0.75$	1039	900	0.689
BOSS CMASS Galaxy	$0.75 < z < 0.90$	325	199	0.786

Table 8
Details of redshift bins in the luminosity function calculation of the BOSS CMASS Sample. The first and second columns are the survey and redshift range respectively. The third column is the total number of objects selected into each respective sample in these redshift ranges. The fourth column is the number of objects actually used in the luminosity function calculation. For the SDSS I/II sample, these two columns are the same. For the BOSS CMASS Sample, there is an additional requirement for objects to pass the fiducial selection cuts defined in term of intrinsic properties described in the text. The last column shows the median redshift of all objects in the third column.

distribution of galaxies in the red portion of the sample, where the sample is complete, allows one to extrapolate and determine the number density in the blue part where the sample is biased against faint objects. The same argument also applies the other way around, allowing one to use the luminous portion of the sample, which is complete in color, to determine the number density at the fainter part where the sample is biased against blue objects. The validity of this assumption is shown in Figure 17, where the number densities (sum of $1/V_{\rm max}$) for the sample are shown for a number of bins in both magnitude and color. The distributions in different bins, once normalized, are the same at the bright and red portions of the sample where the selection is complete. This property of the distribution allows us to infer the number density of objects in the region of parameter space where the selection is incomplete from the region where the selection is complete. There are at least a few tens of objects in each bin near the cutoff line, therefore small number statistics should not have a major effect in the conclusion that the number density is a separable function in color and magnitude.

The correction for this incompleteness is as follows. We define a relevant color-magnitude parameter space given by $C = [5000] - [4200]$ and $M = [5000]$. For each gridpoint in this parameter space, we define the distribution $D(M, C)$ such that $D(M, C)\Delta M\Delta C$ is the comoving number density of post-starburst galaxies with color between C and $C + \Delta C$ and magnitude between M and $M + \Delta M$, which is calculated by summing the inverse $V_{\rm max}$ of all galaxies belonging to that gridpoint.

The number density in grid points that are incomplete because of the selection can then be predicted by extrapolation from the complete part of the parameter space, under the assumption that the distribution is a separable function in magnitude and color. The number density in an excluded grid point, written as $D_{\rm incomplete}(M, C)$, can be calculated from the total number density in three different regions of the parameter space: the part of the parameter space at the same color but with magnitude bright enough to be complete $[\int_{-\infty}^{M_{\rm crit}} D(M', C)dM']$, the part at the same magnitude but with color red enough to be complete $[\int_{C_{\rm crit}}^{\infty} D(M, C')dC']$, and the part that is both red and bright enough to be complete $[\int_{-\infty}^{M_{\rm crit}} \int_{C_{\rm crit}}^{\infty} D(M', C')dC'dM']$. Because the underlying distribution is a separable function in magnitude, the ratio of the first to the third quantities are the same as the ratio of $D_{\rm incomplete}(M, C)$ to the second quantity. This is because the intrinsic shapes of the distribution as a function of magnitude, up to a normalization factor, do not change with color. Another equivalent way to think about this is that the ratio of the second to the third quantities are the same as the ratio of $D_{\rm incomplete}(M, C)$ to the first quantity, because the intrinsic shapes of the distribution as a function of color also do not change with magnitude. Either way, this yields the final expression of $D_{\rm incomplete}(M, C)$ as

$$D_{\rm incomplete}(M, C) = \frac{\int_{C_{\rm crit}}^{\infty} D(M, C')dC' \int_{-\infty}^{M_{\rm crit}} D(M', C)dM'}{\int_{-\infty}^{M_{\rm crit}} \int_{C_{\rm crit}}^{\infty} D(M', C')dC'dM'}. \quad (10)$$

Here $M_{\rm crit}$ is the magnitude where the diagonal selection line in Figure 15 crosses the blue color limit $C = 0.2$, yielding $M_{\rm crit} \sim -23$. The value of $C_{\rm crit}$ is the color cutoff above which the selection is complete. This value depends on the value of magnitude being considered, given by $C_{\rm crit} = \max(0.2, (M + 23.3)/1.8)$. For gridpoints that are on the selection cut and are partially excluded, we calculate the number density distribution by combining the information from objects in the complete part with the predicted distribution for the incomplete part, both weighted by the respective areas of their parts in the cell.

Once the distribution function over the grid has been determined, the luminosity function can be calculated simply by integrating over the color

$$\Phi(M) = \int_{-\infty}^{\infty} D(M, C')dC' \quad (11)$$

where $D(M, C)$ is now the distribution in both color and magnitude corrected for incompleteness from the selection.

Finally, this luminosity function is corrected for another incompleteness due to possible contribution from objects with low signal-to-noise ratio ($S/N < 2$) that may be missed by our selection method (Figure 5) and thus not in the sample. This correction factor is estimated from the fraction of the entire BOSS CMASS galaxy sample that have signal-to-noise ratio lower than 2 in each redshift and rest-frame [5000] magnitude bin used in the luminosity function calculation. Note that the fraction of CMASS galaxies with signal-to-noise ratio

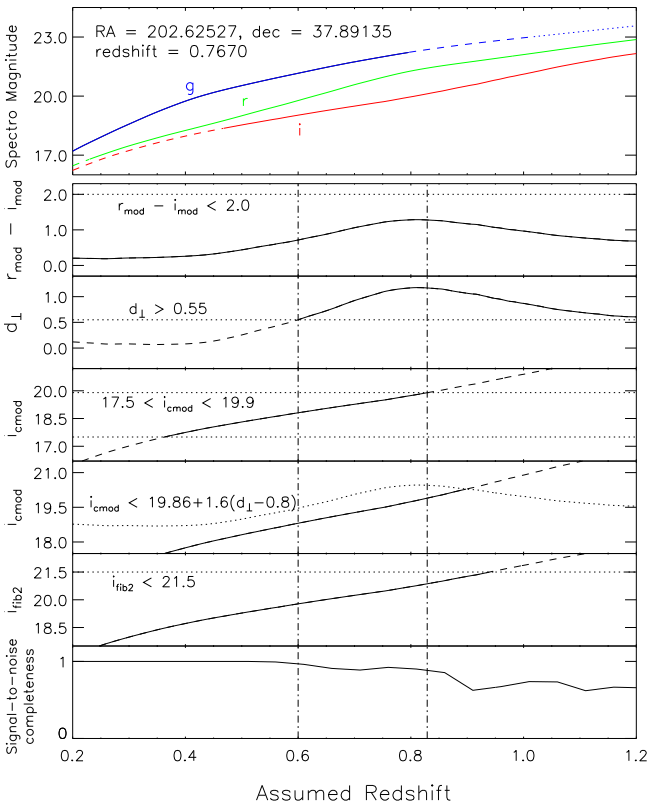

Figure 14. Example to demonstrate our method to calculate $V_{\rm max}$ for a specific BOSS CMASS galaxy. The spectrum of this object is shown in Figure 2. The top panel shows the Spectro magnitude in each of the g, r and i bands that the object would appear to have at any assumed redshift. The solid lines correspond to the redshift ranges over which the magnitude can be calculated directly from the spectrum. Dashed lines correspond to the redshift ranges where the magnitudes are calculated from the best-fit template because the wavelength coverage of the spectrum does not cover the band. The dotted lines correspond to the redshift range where neither the spectrum or the template fit covers the band, and the magnitude is simply extrapolated. The lower five panels show relevant selection criteria used by CMASS evaluated in this redshift range, with the thresholdsshown as dotted lines where relevant. Various kinds of magnitudes are converted from the Spectro magnitude, with extinction taken into account. The relevant quantities in each panel are shown by the solid line in the redshift range where the criteria is met, and dashed line otherwise. The bottom panel shows the signal-to-noise completeness $\mathcal{C}(z)$, which is derived using Monte-Carlo simulation, with details described in the text. The horizontal dotted lines show the selection thresholds. The vertical dash-dotted lines indicate the redshift range where all five selection criteria are met simultaneously, corresponding to the redshift range within which this object will still be selected into the CMASS Sample.

too low to have redshift measurement is very small. The resulting multiplicative correction factor for the CMASS luminosity functions is shown in figure 18 for different redshift bins. It should be noted that the magnitude of this correction is quite small - 20% in the most incomplete redshift and magnitude bin. In fact, the most incomplete bins include no post-starburst galaxies, and thus we do not measure the luminosity function in those bins anyway. The equivalent correction is not performed on the SDSS Main Galaxy Sample, since the signal-to-noise ratios of SDSS galaxies are significantly better than that of CMASS galaxies and we expect the selection biases due to this effect to be insignificant.

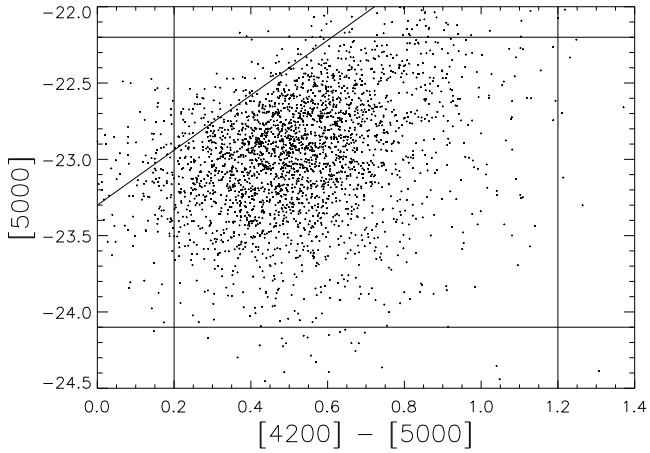

Figure 15. Our post-starburst galaxies from the BOSS CMASS Sample at all redshifts, shown in rest-frame absolute magnitudes and colors calculated from the spectra. The solid lines shown are the selection cuts in this parameter space corresponding roughly to the CMASS selection in term of i and $d_\perp$ at redshift $z \sim 0.5$. At magnitude fainter than $M \sim -23$, the color-dependent magnitude cut introduces an additional selection bias in the luminosity function calculation.

The luminosity function is calculated for our post-starburst galaxies from the BOSS CMASS Sample in four different redshift bins. We imposed lower and upper limits to redshift for the lowest- and highest-redshift bins at $z = 0.45$ and $z = 0.90$, which contain essentially all post-starburst galaxies selected from the BOSS CMASS Sample. The number of objects in each redshift bin is shown in Table 8. The error bar in the luminosity function is calculated using Poisson statistics, and propagated through each successive bias correction factors. However, the error does not take into account possible systematic errors in the correction for color incompleteness.

Figure 19 shows the resulting luminosity functions of BOSS CMASS post-starburst galaxies for all four redshift bins, as well as those calculated from the SDSS I/II sample in two redshift bins. The luminosity bins indicated by filled (empty) symbols in the right panel of the figure have less (more) than 20% of their value of luminosity function contributed by this correction. The SDSS I/II luminosity functions are not shown in empty/filled symbols to indicate the effect of bias correction, since this correction is unique to the BOSS CMASS sample due to its color selection.

These luminosity functions are quite different in different redshift bins; we see strong evidence for redshift evolution. The downsizing trend can be seen in two ways from this plot. The first is that the magnitude where the luminosity function peaks becomes progressively more luminous for higher redshift. This indicates that the typical post-starburst galaxies at higher redshift are more luminous than at lower redshift. However, selection biases can be important here, because the peak magnitudes in each redshift bin are very close to the cutoff magnitudes. We discuss a posteriori tests of the luminosity function below in Section 5.5.

The second way to see the downsizing trend, which is less affected by the selection biases, is to compare number densities of post-starburst galaxies at fixed magnitude for different redshift bins. For example, at $M = -23.5$

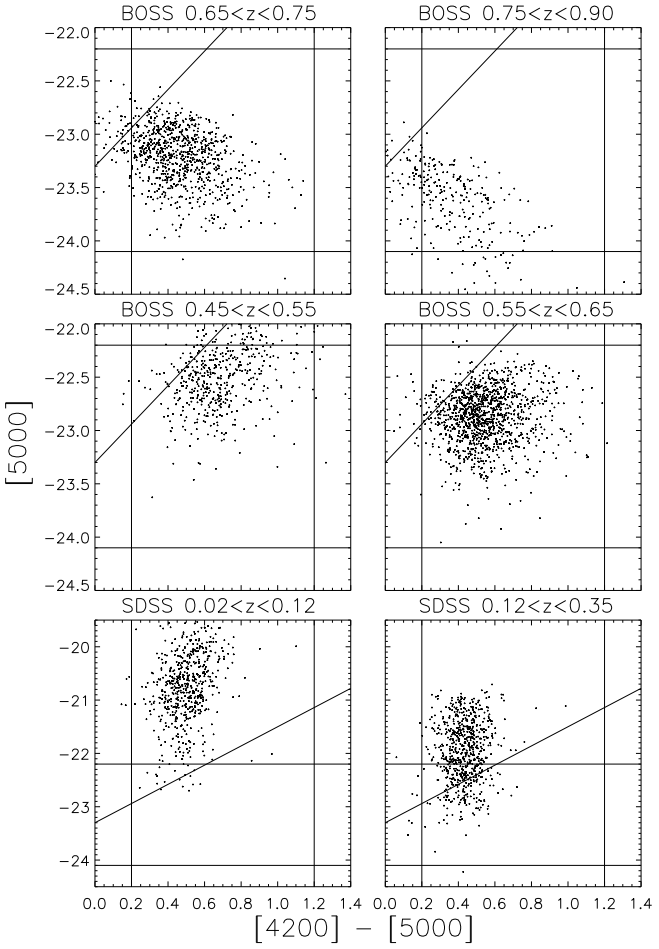

Figure 16. Distribution of our post-starburst galaxies in rest-frame magnitudes and colors similar to Figure 15, but separated into redshift bins. The top four panels show the BOSS CMASS Sample, along with the selection cuts in these quantities. Only objects that pass these selection cuts are used to calculate the luminosity functions. The lower two panels show the equivalent plot for the SDSS I/II Main Galaxy Sample. The selection cuts used in BOSS sample are shown only for comparison for these two panels, but are not used since this sample is not subject to the CMASS selection.

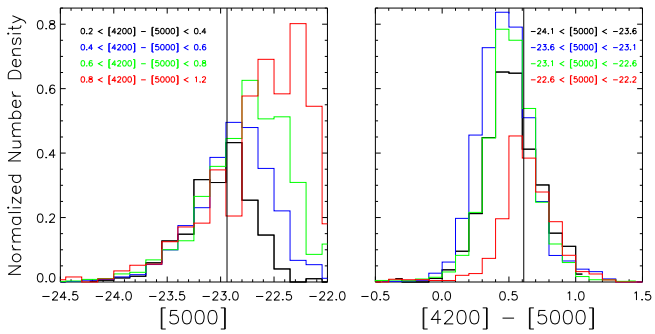

Figure 17. The relative distributions of the number density of galaxies ($\Sigma(1/V_{\rm max})$) as a function of color and magnitude. Left panel: the relative distribution as a function of magnitude for different colors, normalized such that the total numbers of galaxies brighter than $M_{\rm crit}$ (vertical line) is the same for each color bin. Right panel: distribution as a function of colors for different magnitudes, normalized such that total numbers of galaxies redder than $C_{\rm crit}$ are the same for each magnitude bin. With this normalization, the curves are approximately coincident where the distributions are complete, showing that the distributions of galaxies in color and magnitude are indeed approximately separable and independent.

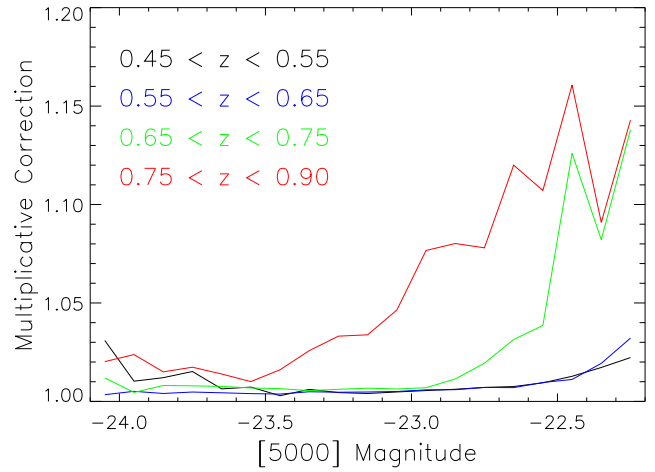

Figure 18. The multiplicative correction factor for the BOSS CMASS luminosity function, to take into account the possible contributions of objects with signal-to-noise ratio $S/N < 2$ which may have been missed by the survey, shown as a function of redshift bin. This correction factor is calculated from the fraction of the CMASS galaxies with signal-to-noise ratios less than two in each respective redshift and rest-frame [5000] magnitude bin.

the number densities for different redshift bins gradually decrease from $z \sim 0.7$ to $z \sim 0.5$, while the two low-redshift bins of SDSS have almost no galaxies at that magnitude, even though they would have been observed and selected if they exist. The exception to this trend is the highest-redshift bin ($0.75 < z < 0.90$) which has the smallest number of galaxies but suffers from the largest selection biases.

This way of viewing the downsizing trend is shown in Figure 21. The number densities at fixed luminosity are shown as a function of redshift. The information used in this plot is the same as that in Figure 19, using magnitude bins of size $\Delta M = 0.5$. For each luminosity, the number density of post-starburst galaxies increases strongly with redshift, by more than an order of magnitude from $z = 0.1$ to $z = 0.6$ in the case of the sample at $M = -23$, while at fixed redshift, the fainter objects are more numerous. The exception to these trends is again the highest-redshift bin and lowest luminosity bin, both of which are likely to be affected the most by selection effects.

We compare the luminosity functions calculated in this work to that presented in other works in the literature and show the result in Figure 20. The lowest redshift bin is compared to the work by Quintero et al. (2004), who calculated luminosity function from low-redshift SDSS post-starburst galaxies in the $^{0.1}i$-band. The high redshift comparison is taken from the work by Wild et al. (2014), who calculated the luminosity function of post-starburst galaxies at redshift $z \sim 1$ at the rest-frame 1μm in the UDS field. We convert all luminosity functions to a common rest-frame wavelength at 5000Å ([5000] band). We found that the luminosity functions in our work broadly agree at the low-redshift bin with what Quintero et al. (2004) found, but is roughly a factor of 5-10 lower than that of Wild et al. (2014) in the overlap-

ping magnitude range in the highest-redshift bin. Our luminosity function in the second-highest redshift bin shows more agreement with the result from Wild et al. (2014). The disagreement in the highest-redshift bin may reflect the selection bias and incompleteness at this redshift. The differences in wavelength bands, surveys and sample selections likely contribute to this disagreement as well. It should also be noted that the stellar masses of our post-starburst galaxies in different redshift bins are likely vastly different. This is because the color selection of the CMASS sample is designed to isolate massive galaxies - and is incomplete at redshift $z > 0.6$ and $M_* < 10^{11} M_\odot$ (Maraston et al. 2013; Leauthaud et al. 2016) - while the SDSS Main Galaxy Sample target more intermediate mass galaxies. Our selection bias correction should correct for part of the CMASS stellar mass incompleteness, but since we are working in term of absolute magnitude instead of stellar mass, it is not clear how much has been corrected for.

The luminosity functions confirm that luminous post-starburst galaxies are indeed a rare class of objects, with a space density $\Phi_{\rm PSG} \sim 10^{-(6-7)}\,{\rm Mpc}^{-3}{\rm mag}^{-1}$ at $M \sim -23$. For comparison, the space density of early-type galaxies at the knee of their luminosity function is about $\Phi_{\rm EG} \sim 10^{-3}\,{\rm Mpc}^{-3}{\rm mag}^{-1}$ (Bell et al. 2004; Baldry et al. 2004).

We find that the luminosity functions of the BOSS CMASS galaxies generally increase toward fainter magnitudes, as is generally the case for other classes of galaxies. The general shapes, except for the points dominated by large selection bias correction, are reasonably fit with Gaussian functions in magnitude (log-normal functions in luminosity). We thus fit the luminosity functions with half-Gaussians which are constant at magnitudes fainter than the peak. This functional form does not decrease at the faint end; note that our luminosity dynamic range extends only a little below the Gaussian peak. This function has the same number of free parameters as the Gaussian function, and is written as

$$\Phi(M) = \begin{cases} A \exp\left[-\frac{(M-M_0)^2}{\sigma^2}\right] & , M < M_0 \\ A & , M \geq M_0 \end{cases} \qquad (12)$$

The two free parameters in this fit are the normalization A and the peak magnitude M_0, while the width of the Gaussian σ is fixed to be 0.4 magnitude at all redshifts; empirically, the width is very close to constant. With σ fixed, the normalization A is proportional to the total number density in each redshift bin. The fit parameters as functions of median redshift of the bins, along with a linear fit of these parameters as a function of redshift, are shown in Figure 22. This plot shows the trend that we already described; the overall normalization decreases while the peak magnitude becomes brighter at higher redshift.

We also attempted to fit the standard Schechter function (Schechter 1976) to the luminosity function, but we found it to be a poor fit. In the high-redshift bins, we have insufficient dynamic range to meaningfully constrain the power-law index, since our magnitude range only samples the exponential cutoff. Meanwhile, at the low-redshift bins for SDSS I/II, the luminosity functions do not decrease exponentially at the bright end as the Schechter function requires.

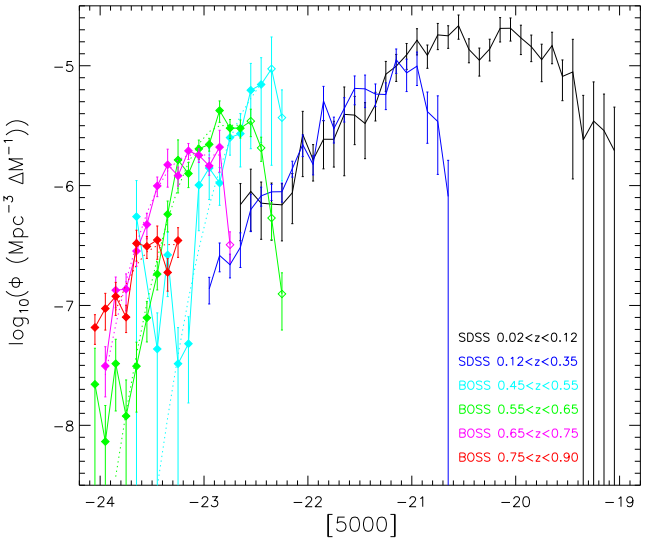

Figure 19. Luminosity functions of the post-starburst galaxies from both the SDSS I/II Main Galaxy Sample and the BOSS CMASS Sample for each of our redshift bins. For the BOSS CMASS Sample, a luminosity bin indicated by a filled (empty) symbol has the CMASS color selection correction contributing to less (more) than 20% of the value of the luminosity function in that bin. The half-Gaussian fits (Equation 12) to the luminosity function for the BOSS CMASS sample are shown as dashed lines. Error bars shown are Poisson.

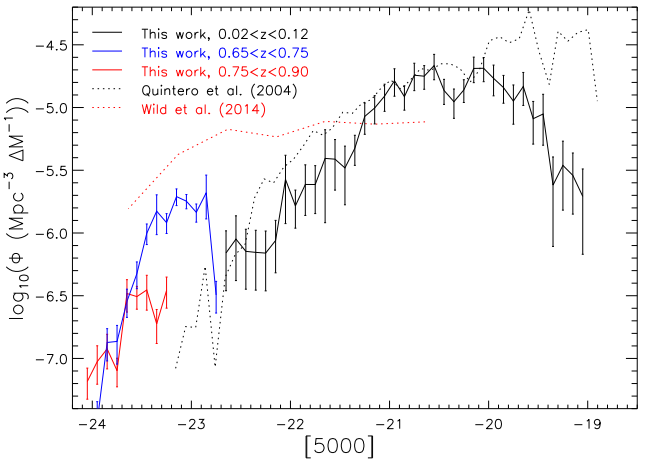

Figure 20. Comparison between post-starburst galaxy luminosity functions calculated in this work to other works in the literature. The solid black, blue and red lines show the luminosity functions from the SDSS Main Galaxy Sample in the redshift bin $0.02 < z < 0.12$ and from the BOSS CMASS Sample in the redshift bin $0.65 < z < 0.75$ and $0.75 < z < 0.90$ respectively. The dotted lines show the comparable luminosity functions from the literature. The black dotted line is the luminosity function of post-starburst galaxies in local universe calculated in the $^{0.1}i$ band, taken from Quintero et al. (2004). The red dotted line is the luminosity function of post-starburst galaxies at redshift $z \sim 1$ at rest-frame 1μm, taken from Wild et al. (2014). The unit of Φ are converted to ${\rm Mpc}^{-3}$ mag^{-1}, with Hubble constant assumed to be $h = 0.7$. The luminosities, measured at different wavelengths in different papers, are converted to [5000] (rest-frame 5000Å) using a sensible stellar population fit that represents a generic post-starburst galaxy spectrum.

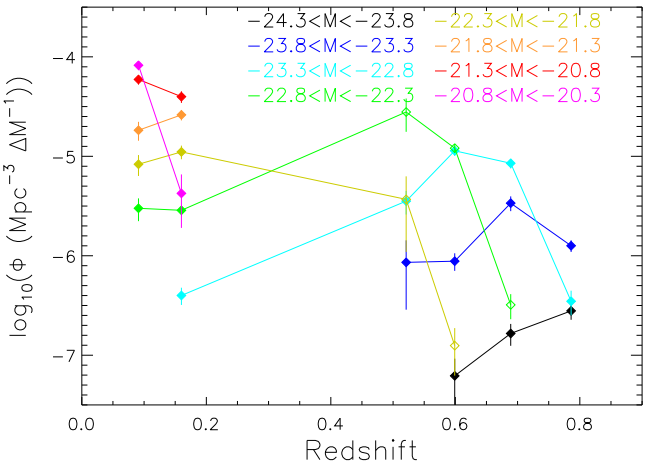

Figure 21. Number density as a function of redshift at fixed luminosity. Each line corresponds to the range of luminosity indicated in the legend, all with width $\Delta M = 0.5$. The error bars are Poisson. This plot contains the same information as in Figure 19 but re-binned in luminosity and plotted as a function of redshift. As in Figure 19, empty symbols indicate points affected significantly by the CMASS color selection correction.

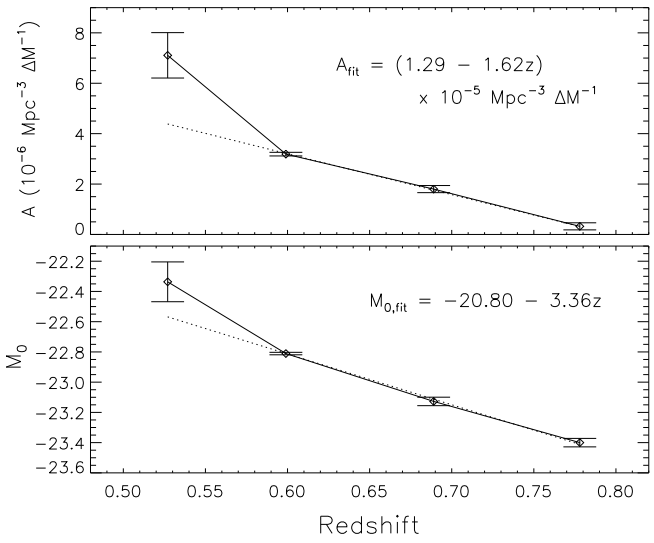

Figure 22. Best fit parameters of the luminosity functions of post-starburst galaxies from our BOSS CMASS Sample for the different redshift bins shown in Figure 19. The fitting function is half-Gaussian, as described in Equation 12, where the normalization A and the peak magnitude M_0 are free parameters and the width is fixed as constant at $\sigma = 0.4$. The dotted lines show the linear fit to these parameters. The redshift on the abscissa is the median redshift of objects in the bin. The empirical linear fits for these parameters are given in each panel.

5.5. *Self-Consistency Test of Luminosity Function from the BOSS CMASS Sample*

The validity of the luminosity function is tested in this section with the method described in, for example, Sandage et al. (1979) and Koranyi & Strauss (1997). Given the measured luminosity function and the observed redshift and SED of each galaxy, one can predict what the luminosity distribution of the galaxies in the sample would be, with color and magnitude selection taken into account. The predicted luminosity distribution can then be compared to the observed one. If the sample is uniform and the measurement is done consistently, the predicted and observed luminosity distributions should agree well. This method is equivalent to asking the question "For a given luminosity function and our selection function, what is the probability distribution of luminosities for a galaxy of a given redshift and SED shape?"

For each galaxy in the sample, the contribution of this galaxy to the luminosity distribution bin is given by

$$P_{\text{one galaxy}}(M)\Delta M = \frac{\Phi(M)S(M)\mathcal{C}(M)\Delta M}{\Sigma\Phi(M)S(M)\mathcal{C}(M)\Delta M}, \quad (13)$$

where $\Phi(M)$ is the luminosity function. The signal-to-noise completeness factor $\mathcal{C}(M)$ for each value of M is calculated by a Monte-Carlo simulation similar to that described in Section 5.4, with the spectrum scaled to that magnitude. The selection function $S(M)$ is the fraction of the sample that could be observed at magnitude M given the color cuts. This is determined from the subsample at $M < M_{\text{crit}}$ where the sample is complete, which has the same color distribution as the rest of the sample, as shown in Figure 17. At fainter magnitudes, only a fraction $S(M)$ of this distribution is left due to the selection cut $M = -23.3 + 1.8C$. $S(M)$ can be written as

$$S(M) = \frac{\int_{C_{\text{cut}}(M)}^{\infty}\int_{-\infty}^{M_{\text{crit}}} D(M',C')dM'dC'}{\int_{-\infty}^{\infty}\int_{-\infty}^{M_{\text{crit}}} D(M',C')dM'dC'} \quad (14)$$

where $C_{\text{cut}}(M) = (M + 23.3)/1.8$.

The predicted luminosity distribution is then derived by summing Equation 13 over the entire sample (or over redshift shells). The final profile of the predicted distribution integrates to exactly the same number of objects in the sample, since the normalization for each object is forced to be unity (as shown in Equation 13).

This method in its simplest form assumes an unchanging population, which is in contrast to the strong redshift evolution we found in Sections 5.3 and 5.4, and the fast drop in the global star formation rate of the universe since redshift unity. To address this issue, we need to take into account the redshift evolution of the luminosity function. For each galaxy, we evaluate the luminosity function $\Phi(M)$ at its observed redshift using the fit parameters to the redshift evolution of the luminosity function shown in Figure 22. This modified method is performed for the BOSS CMASS Sample, both for the whole sample and in redshift bins. The predicted and observed luminosity distributions are shown in Figure 23. They agree very well, giving us an a posteriori confirmation of the robustness of our luminosity function calculation.

It should be noted that, in its simplest form in which both the luminosity function and luminosity distribution are calculated in a narrow redshift bin, this method for self-consistency check employs a circular argument. This is because the underlying population is assumed based on the luminosity function, then the selection effects are imposed to predict the sample one would observe, which is exactly the reverse process of calculating the luminosity function in the first place. However, what breaks the circularity in this case is that now multiple redshift bins

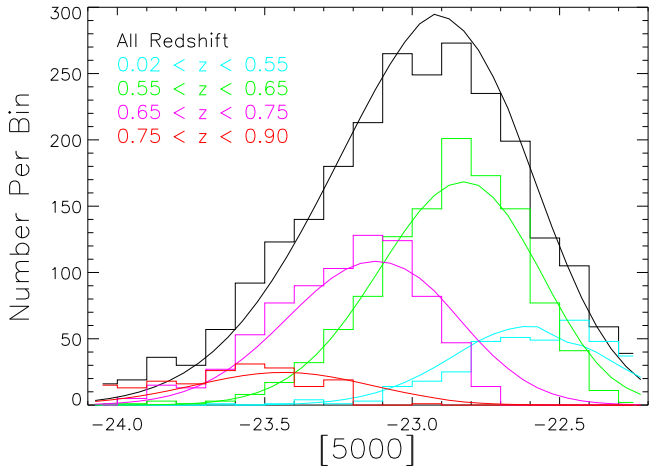

Figure 23. Comparison between the predicted and observed luminosity distribution in the [5000] band of the BOSS CMASS Sample. The histograms show the observed luminosity distribution (simply numbers of galaxies in each magnitude bin). The solid lines are the predicted distribution calculated by the method described in the text. This calculation is performed for both the whole sample (black) and in redshift bins (colored). The agreement between the two is an a posteriori confirmation of the validity of our luminosity function determination.

are linked together through the parametrization of the luminosity function as a function of redshift. The rapid redshift evolution is not assumed because the luminosity function is calculated individually for each redshift bin. Therefore the fact that the overall luminosity distribution of the whole sample, calculated from the evolving luminosity function across 4 redshift bins, agrees with the actual sample is non-trivial.

5.6. *Comparison to Global Star Formation Rate*

We now investigate whether the numbers of post-starburst galaxies in our sample could explain the decrease in the global star-formation rate since redshift $z \sim 1$. In other words, we test whether all the observed decrease in the star-formation rate is purely due to quenching of massive galaxies that are in our sample. In particular, we calculate the mass density in A-stars ($\rho_{\rm A}$, in unit of $M_\odot/{\rm Mpc}^3$) as a function of redshift using both approaches.

The first approach is to calculate the A-star mass density from the post-starburst galaxy luminosity functions, calculated from our sample in Sections 5.3 and 5.4. This is done by performing the integral

$$\rho_{\rm A} = \left(\frac{M}{L}\right)_{\rm A} \left(\frac{A}{\rm Total}\right) \int L\,\Phi(M)\,dM \qquad (15)$$

This entire calculation is performed in our fiducial top-hat band in the wavelength range 4950-5100Å, which we have used in our calculation of the luminosity function. The integral represents the total stellar luminosity density in this wavelength band, with luminosity L consistently calculated from magnitude M in this band. This is then converted to A-star luminosity density with the global fraction $A/{\rm Total} \sim 0.26$, which is calculated from fitting the templates to the coadded spectrum of the entire sample. Note that this $A/{\rm Total}$ value here is calculated in the [5000] band, and is not the same as the one used in the selection algorithm, which is in the [4200] band, which explains the low value. Finally it is converted to A-star mass density with the mass-to-light ratio of A-stars, which is calculated from the spectrophotometrically-calibrated spectrum of Vega by Bohlin & Gilliland (2004), assuming the distance to Vega of 7.68 pc.

The second approach is to calculate the A-star mass density expected from the declining global star-formation rate $\rho_{\rm SFR}$. This is done by integrating the excess star-formation rate backward in time in the time interval that would result in the stellar population being identified as post-starburst by our definition at the epoch under consideration.

$$\rho_{\rm A}(t) = \left(\frac{M_{\rm A}}{M_*}\right) \int_{t-\tau_1}^{t-\tau_2} (\rho_{\rm SFR}(t') - \rho_{\rm SFR}(t-\tau_1))\,dt' \qquad (16)$$

The global star-formation density $\rho_{\rm SFR}$ (in unit of $M_\odot {\rm yr}^{-1}{\rm Mpc}^{-3}$) as a function of redshift is calculated using the fit formula in Equation 15 from Madau & Dickinson (2014). The fraction $M_{\rm A}/M_* \sim 0.07$ is the ratio of A-star mass to total mass formed. This is calculated from the Salpeter initial mass function (which is the same IMF assumed in the formula) assuming the lower and upper limits of A-star mass to be $1.6 - 2.9 M_\odot$ respectively, while limiting the stellar masses to be between $0.08 - 100 M_\odot$. The parameters τ_1 and τ_2 are the lower and upper age of the stellar population that would be identified as post-starburst by our selection algorithm. The lower limit, $\tau_1 = 50$ Myr, corresponds to the lifetime of a B3 star, which is the lowest mass star able to produce an HII region around it, leading to significant [OII] emission. The upper limit, $\tau_2 = 800$ Myr, is derived by comparing the single stellar population model by Maraston (2005) to our selection, requiring the A/Total ratio to be larger than 0.25. This age range, 50-800 Myr, is similar to the interval between the ages of B-stars and A-stars, as one would intuitively expect.

One inherent assumption in this estimate is that all galaxies that are still forming stars at the end of the time window were also forming stars at the beginning, and therefore are not in the post-starburst population. However, it can be the case that additional galaxies have quenched during that time period, joining the post-starburst population, while more star-formation happens in other galaxies to compensate for the overall star-formation rate. Thus this estimate is a conservative lower limit, since it only shows the minimum amount of quenching demanded by the declining global star-formation rate.

We performed this exercise of estimating the A-star mass density by these two different methods in all redshift bins we used to calculate the luminosity function. This is shown in the upper panel of Figure 24. We define the parameter η, shown in the lower panel of the same figure, as the ratio between the mass density of A-stars required by the global star-formation rate to that calculated from luminosity functions. This parameter, which has typical values of around 100, suggests that the massive post-starburst galaxies in our sample account for

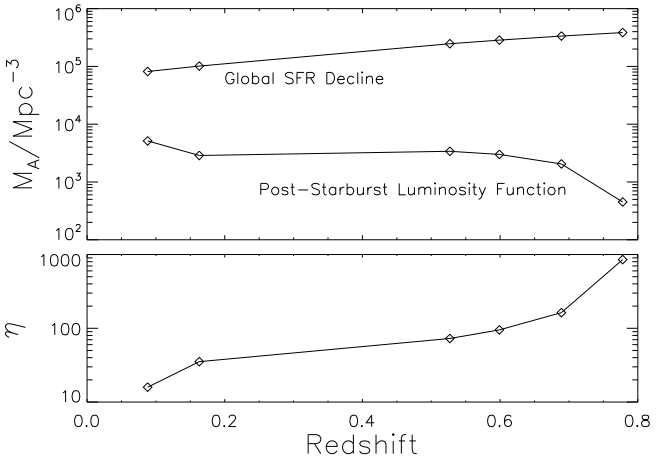

Figure 24. Top panel: The mass density in A-stars as a function of redshift (in units of $M_\odot/\mathrm{Mpc}^3$) calculated in two ways. The bottom line is calculated from the luminosity functions of post-starburst galaxies in our sample. The top line is what expected from the declining global star-formation rate, as quantified by Madau & Dickinson (2014). Bottom panel: The ratio of the densities shown in the top panel. The typical value of around 100 indicates that the star formation quenching in massive post-starburst galaxies is a small component of the total decline of star formation in the universe.

only a small component of the decline of star formation in the universe. The vast majority of this decline must be either in lower luminosity post-starburst galaxies, or in systems in which the star formation declines only gradually.

Indeed, this calculation contains a number of simplifying assumptions. For example, the A/Total ratio, while assumed to be global, can potentially be a function of luminosity. The IMF is simply assumed to be Salpeter. The mass-to-light ratio of A-stars are taken from Vega which is an A0 star and therefore is not representative of the whole A-star population. In addition, the luminosity functions we have calculated may still have residual selection biases despite all the corrections we have performed, especially in the highest redshift bin. Each of these assumptions might easily give a factor of two error to the calculation. However, given that the discrepancy between the mass density of A-stars calculated from these two different methods is about two orders of magnitude, our qualitative conclusion is robust to these uncertain details.

6. DISCUSSION

6.1. *Sample*

From the publicly available data from the Sloan Digital Sky Survey, we have identified a large number of post-starburst galaxies based on their optical spectra. This sample is the largest sample of post-starburst galaxies thus far, and consists of 2359 galaxies from SDSS I/II and 3964 galaxies from SDSS III (BOSS) respectively. The highest-redshift objects are at redshift $z \sim 1$ and $z \sim 1.3$ for the two surveys respectively. In fact, for the BOSS sample, the size of the sample can be increased significantly: the sample used in this work is selected from the Ninth Data Release (DR9; Ahn et al. (2012)), while the BOSS survey now contains twice as many spectra (DR12; Alam et al. (2015)). This sample provides a valuable observational foundation for galaxy evolution studies.

The stellar populations of post-starburst galaxies are modeled with two main components: young A-stars and an old underlying component. They are selected to not have any indication of ongoing star formation as measured by [OII]λ3727 nebular line emission. So these objects had a large amount of star formation between 50 million and 0.8 billion years previously that is almost entirely quenched by the epoch when they are observed.

Their spectra also show a diverse range of features. Weak MgII absorption is seen in a large number of objects. This feature is related to the intragalactic gas, and its velocity relative to the systemic redshift indicates inflow or outflow. A small number of objects show either blue continuum or broad MgII in emission, both of which are related to AGN activity which is thought to be one possible feedback mechanism to cause the quenching.

6.2. *Evolution of the Luminosity Function*

The luminosity functions calculated from the SDSS I/II and BOSS samples in a number of redshift bins evolve rapidly over the redshift baseline from $z \sim 0.8$ to 0.1. The sense of this evolution is consistent with downsizing, where the typical stellar mass of objects that are currently quenching their star formation decreases with cosmic time (e.g., Bundy et al. (2006)).

This dramatic evolution is expected in light of the finding that the global star formation rate of the universe drops by an order of magnitude since redshift $z \sim 1$ (Madau & Dickinson 2014). The decrease in global star formation rate would require a number of star-forming galaxies to be quenched. These galaxies would subsequently enter the post-starburst phase, in the redshift range we probe with this survey. Under the assumption that all galaxies pass through a post-starburst phase after quenching, and that our sample selection is sufficiently complete, we would expect that the evolution in the luminosity function of post-starburst galaxies should broadly reflect the evolution in global star formation rate.

To check this idea, we calculated the mass density in A-stars indicated by the measured luminosity functions, and compared this to what is expected from the declining global star-formation rate. We found that the mass density of A-stars in our post-starburst galaxies is smaller than that expected by a factor of ~ 100, suggesting that most star-forming galaxies at high redshift do *not* go through a luminous post-starburst phase, and post-starburst galaxies are indeed a rare occurrence.

In light of this result, there are a few ways in which the star formation rate could decrease without entering the post-starburst phase. The first is that most of the star-formation quenching might happen in low-mass galaxies or satellites that are not luminous enough to be selected as part of the survey. The $1/V_{\mathrm{max}}$ formulation we performed in redshift bins does not correct for this because the luminosity functions are evolving with redshift, and thus faint galaxies that are seen locally can not be used to infer the corresponding population at higher redshift. Indeed, even if there exists a large population of unseen low-luminosity galaxies at high redshift, it would not contribute much to the total luminosity and inferred mass. For example, if the faint end of the luminosity function at $0.65 < z < 0.75$ mirrored that of the $0.02 < z < 0.12$ bin, it would increase the total luminosity in that bin by

less than a factor of 2.

The second way this could happen is for the star formation to be quenched gradually in the majority of star-forming galaxies, and perhaps staying at a modest rate thereafter (e.g. Cortese & Hughes 2009; Salim et al. 2012; Fang et al. 2012, 2013; Schawinski et al. 2014). Such galaxies will never show a strong A-star component in their spectra, and will not be identified as a post-starburst galaxy. We believe that this scenario is the main channel by which the star-formation rate in the universe has decreased, given that reasonably massive galaxies, like our Milky Way, that retain modest levels of star formation are common.

Another complication in this aspect is that a fraction of post-starburst galaxies might not represent a key evolutionary stage of the galaxy, but only a random, stochastic phase of a small-scale starburst which is not significant compared to the total stellar mass of the galaxy. Depending on the exact details of the selection criteria, these objects might pass through the selection and enter the sample. This issue can be answered, again, by understanding the mapping between the fundamental properties of the stellar population to the observable spectral features, which can be done with stellar population synthesis models.

6.3. *Mechanisms Responsible for Quenching*

Another key aspect is the physical mechanism for quenching the star formation on a short timescale. There are two main scenarios by which this can happen. The first involves cluster-related mechanisms such as ram-pressure stripping, in which a star-forming galaxy falls into a galaxy cluster, and interacts with the intra-cluster medium. The second is the merger-related scenario, where a merger between two gas-rich galaxies induces a large starburst which is subsequently quenched either due to feedback or gas exhaustion. These scenarios can be distinguished in a number of different ways, some with data available in this sample, some requiring more complementary information.

One possible way to approach this would be to use stellar population model fits to the individual galaxy spectra to reconstruct a crude star-formation history of each galaxy. If the recent star formation history is consistent with a large starburst that is quenched quickly, then it would be more consistent with the merger scenario where the large scale starburst is induced all at once, possibly at the center of the galaxy. In contrast, if the star-formation history is closer to being constant, before being quenched relatively suddenly, then it would be closer to the cluster interaction scenario. In this case, the term post-starburst is certainly misleading, because there is no burst, but it can have a strong enough A-star feature to be classified under this group if the star formation is quenched suddenly enough (Quintero et al. 2004). In practice, distinguishing these two scenarios in stellar populations is a challenging task and might only be possible for extreme cases even for a high signal-to-noise ratio spectra.

Another clue contained within the spectra is the presence of AGN, which certainly also can play an important role in the evolution of the galaxy, and might be closely related to how the star formation is quenched. Simulations (Hopkins et al. 2006, 2008; Sijacki et al. 2007) invoke the quenching from AGN feedback, providing the energy needed to stop overproduction of stars. However, there is evidence (Wild et al. 2010; Shin et al. 2011; Yesuf et al. 2014) that AGN activity tends to peak after the starburst end, and therefore might not be the cause of star formation quenching. Quantifying the number of post-starburst galaxies with spectroscopic AGN signatures might yield an understanding of the influence central AGNs have on this population. In our sample there are ~ 100 objects that show signs of AGN activity such as blue continuum or, more importantly, broad line emission. However, this number might suffer from severe selection bias, since AGN activity can give rise to [OII]λ3727 emission, leading to exclusion of objects from our sample. Potentially, one can also use emission line diagnostics (BPT diagram; Baldwin et al. (1981); Veilleux & Osterbrock (1987)) to identify obscured AGN that do not show broad-line emission. In addition to the optical signature of the AGN, if complementary data in other wavelength ranges (such as X-ray or radio) is available then one might also have different ways to detect and quantify AGN properties and understand this relation (e.g. Shin et al. (2011)).

Moreover, this sample can be augmented by a number of external datasets. Firstly, deep imaging data can be very useful to quantify the environment of the post-starburst galaxies, i.e., whether they lie in galaxy clusters or the field. The requirement is that these imaging data have to be deep enough to see a typical L_* galaxy at redshifts up to unity. The SDSS photometric data are not deep enough to do this, but various current and upcoming weak-lensing surveys such as the Canadian-France-Hawaii Telescope Legacy Survey (CFHTLS; Heymans et al. (2012)), the Dark Energy Survey (DES; The Dark Energy Survey Collaboration (2005)), Hyper-Suprime Cam (HSC; Miyazaki et al. (2012)) and the Large Synoptic Survey Telescope (LSST; Ivezic et al. (2008)) would be sufficient for this task.

High resolution HST imaging data would also be useful in studying the morphology of these objects at high redshift to probe the effect of close interactions and mergers, possibly by comparing to a control sample of normal galaxies with similar mass and redshift. If a significant fraction of post-starburst galaxies, especially ones in the field, show signs of disturbed morphology or close, merging neighbors, it would lend support to the merger scenario. It would also be interesting if one finds field post-starburst galaxies with smooth morphology, since that would need some other explanation. There are a number of works studying morphologies at low redshift (e.g., Yang et al. (2008) for post-starburst galaxies, Cales et al. (2011) for post-starburst quasars). However, since the post-starburst galaxy population at high redshift is significantly different from that at low redshift, as seen in the evolution of the luminosity function, independent studies at high redshift must be done to fully understand the properties and mechanisms at work in the high-redshift population.

Indeed, the single most important piece of information that would allow us to explore different ways that galaxies evolve is the stellar mass. This is because the observed color and luminosity change in complex ways due to stellar evolution, while the stellar mass reflects fundamental changes in galaxy properties like mergers, infall or star formation. In general, the stellar mass can be determined

by spectral fitting up to a factor of a few. However, it should be noted that the post-starburst stellar population may be dominated by the relatively less-understood TP-AGB stars, and therefore the error in determining stellar mass might be larger.

6.4. *Improvement to Selection Method*

In this work, we have developed a robust method to select post-starburst galaxies from optical spectra. This method relies minimally on prior knowledge of the redshift of the object, making it suitable to apply to large amounts of spectroscopic data even in the presence of large redshift errors in the standard pipeline. This algorithm selects a relatively small number of candidates from the large dataset for visual inspection to confirm the correctness of the identification. While the false negative rate is very small based on a small test sample of known post-starburst galaxies, the false positive rate to be removed by visual inspection is between 100% and 300%. At this point, the amount of visual inspection required is still manageable, but more optimized algorithm with lower false positive rate will be critical when the next generation of surveys generate significantly larger samples. Examples of such surveys are the fourth phase of the Sloan Digital Sky Survey (SDSS IV; Dawson et al. (2015)), The Dark Energy Spectroscopic Instrument (DESI; Levi et al. (2013)) and the Prime Focus Spectrograph (PFS; Takada et al. (2014)). For SDSS and BOSS data in particular, it was found in retrospect that the redshift determination by the spectroscopic pipeline is very robust, with less than 5% incorrect redshifts even for this rare class of objects. Therefore, selecting the post-starburst galaxies from SDSS and BOSS assuming the pipeline redshifts to be reliable would have simplified the process and reduced the number of false positives significantly.

In light of this, there are some improvements to incorporate the future work selecting post-starburst galaxies from large spectroscopic surveys. One such dataset in the near future would be the entire BOSS survey (SDSS DR12). This phase of SDSS contains twice as many spectra than what we used in this paper, and is now public (Alam et al. 2015).

The first improvement might be to do the selection based on the stellar population properties, rather than empirical cuts on parameters such as A/Total or equivalent widths. Ideally, this approach is more preferable since it would lead to selection based on physically meaningful properties of the galaxy population such as stellar population age and metallicity. For example, one might define post-starburst galaxies to be populations that are older than 300 Myr but younger than 1Gyr. Yesuf et al. (2014) fit stellar population models using multi-wavelength data while taking AGN and dust obscuration into account.

Selection of these objects from the next generation of multi-band photometric surveys is another possibility. Doing so requires distinguishing between the 3600Å Balmer break and the 4000Å break at slightly different redshifts. One can potentially resolve this ambiguity using multi-wavelength information, for example in NUV and NIR, since the old population would have almost no flux in NUV but large flux in NIR, and conversely for the young population. Wild et al. (2014) studied galaxy SEDs in optical and NIR, and found that post-starburst galaxies have unique, identifiable colors. However, the presence of dust and AGN would make this task challenging.

7. CONCLUSION

The post-starburst phase is a rare phase in galaxy evolution, in which a small number of star-forming galaxies are on their way to becoming passive early-type galaxies. Therefore, understanding this class of galaxies could yield clues about how galaxies evolve and the mechanisms that drive evolution, at least for massive galaxies. Currently, there are many open questions in this topic, ranging from phenomenological aspects such as the luminosity function and its evolution with redshift, to the physical mechanisms that cause star formation to stop and subsequently turn a star-forming galaxy into a post-starburst galaxy. One key limitation faced by many previous works was the lack of a large, statistical sample with uniform selection over a broad range of redshift.

In this paper, we have systematically selected a sample of post-starburst galaxies from the SDSS DR9 spectroscopic dataset. The method we developed is based on template fitting, with cuts on equivalent widths applied to various relevant spectral lines. The selection algorithm is tested and verified against a smaller sample of post-starburst galaxies known prior to the study. All objects in the final sample are visually inspected to remove false positives.

We apply this selection scheme to the entire SDSS DR7 spectroscopic database, and also to the BOSS spectroscopic dataset presented in DR9. This yields 2330 galaxies from the SDSS DR7 dataset, and 3964 galaxies from the BOSS dataset. This is the largest sample of post-starburst galaxies currently available in the literature. The full list of these objects is available with this paper. The redshifts of these galaxies range from local galaxies up to $z \sim 1.3$, with a median redshift of ~ 0.16 and ~ 0.61 for the SDSS DR7 and BOSS subsamples respectively, with little overlap between them. Various interesting spectral features are seen, such as MgII absorption in a large number of galaxies, and broad MgII emission and blue continuum in about 100 objects. They are the so-called post-starburst quasars.

A large fraction of SDSS DR7 sample is selected by the Main Galaxy Sample, while the dominant spectroscopic selection algorithm for BOSS sample is CMASS. These two subsamples have uniform magnitude and color selection criteria, allowing us to calculate luminosity functions in a number of redshift bins.

We quantify and correct for various selection biases in the luminosity function calculation. The first bias is the different cosmological volume over which each object can be selected from the spectroscopic sample of the survey. This is corrected by the standard $1/V_{\rm max}$ method, where $V_{\rm max}$ is calculated from the individual spectrum and the details of the selection criteria for each subsample. The second effect is due to the color selection algorithm used in the CMASS Sample, which is biased against faint blue objects, even though we expect post-starburst galaxies to also exist in that region of color space. This is corrected by extrapolation from the complete part of the color distribution, assuming that the underlying distribution is

separable in color and magnitude, an assumption shown to be consistent with the data. Moreover, after all the corrections are performed, we compare the observed distribution of objects in luminosity to the expected one given the luminosity function. The observed and expected distributions are consistent, suggesting that our method to calculate the luminosity function is robust.

We see strong redshift evolution of the resulting luminosity function of our post-starburst galaxy sample. The sense of this evolution is that the number density at fixed luminosity of post-starburst galaxies is considerably higher at high redshift. In other words, we see the "downsizing" trend in the luminosity function evolution that has been seen in other galaxy populations. At fixed redshift, the less luminous objects are more abundant than luminous objects. This trend, qualitatively, is in line with the expectation from the fact that the global star formation rate of the universe has dropped by about an order of magnitude since redshift $z \sim 1$.

We performed a quantitative comparison between the mass density of the post-starburst A-star population from our sample (by integrating over the luminosity function), to that expected from the declining global star-formation rate. We found that only a small fraction, approximately 1%, of the minimum star-formation quenching required by the declining global star-formation rate, can be explained by the amount found in post-starburst galaxies. This makes post-starburst galaxies a rare phenomenon. It suggests that most star-formation quenching has to happen in ways that escape our post-starburst galaxy selection method. This can be either by quenching gradually enough to never show strong post-starburst spectral signatures, or by quenching in low-mass galaxies or satellites that are too faint to be selected into the SDSS survey at high redshift.

ACKNOWLEDGEMENTS

We thank Kevin Bundy, Renyue Cen, Jenny Greene, James Gunn, Robert Lupton, and Christy Tremonti for useful discussions, insights and comments during the entire duration of this project. We also thank the anonymous referee for exceptionally thorough feedback, which has improved the paper significantly.

Funding for SDSS-III has been provided by the Alfred P. Sloan Foundation, the Participating Institutions, the National Science Foundation, and the U.S. Department of Energy Office of Science. The SDSS-III web site is http://www.sdss3.org/.

SDSS-III is managed by the Astrophysical Research Consortium for the Participating Institutions of the SDSS-III Collaboration including the University of Arizona, the Brazilian Participation Group, Brookhaven National Laboratory, Carnegie Mellon University, University of Florida, the French Participation Group, the German Participation Group, Harvard University, the Instituto de Astrofisica de Canarias, the Michigan State/Notre Dame/JINA Participation Group, Johns Hopkins University, Lawrence Berkeley National Laboratory, Max Planck Institute for Astrophysics, Max Planck Institute for Extraterrestrial Physics, New Mexico State University, New York University, Ohio State University, Pennsylvania State University, University of Portsmouth, Princeton University, the Spanish Participation Group, University of Tokyo, University of Utah, Vanderbilt University, University of Virginia, University of Washington, and Yale University.

This work is partially based on observations obtained with the Apache Point Observatory 3.5-meter telescope, which is owned and operated by the Astrophysical Research Consortium.

REFERENCES

Adelman-McCarthy, J. K. et al. 2008, ApJS, 175, 297
—. 2007, ApJS, 172, 634
Ahn, C. P. et al. 2012, ApJS, 203, 21
Alam, S. et al. 2015, ApJS, 219, 12
Anderson, L. et al. 2012, MNRAS, 427, 3435
Baldry, I. K., Glazebrook, K., Brinkmann, J., Ivezić, Ž., Lupton, R. H., Nichol, R. C., & Szalay, A. S. 2004, ApJ, 600, 681
Baldwin, J. A., Phillips, M. M., & Terlevich, R. 1981, PASP, 93, 5
Balogh, M. L., Miller, C., Nichol, R., Zabludoff, A., & Goto, T. 2005, MNRAS, 360, 587
Balogh, M. L., Navarro, J. F., & Morris, S. L. 2000, ApJ, 540, 113
Bekki, K., Couch, W. J., Shioya, Y., & Vazdekis, A. 2005, MNRAS, 359, 949
Bekki, K., Owers, M. S., & Couch, W. J. 2010, ApJ, 718, L27
Bekki, K., Shioya, Y., & Couch, W. J. 2001, ApJ, 547, L17
Bell, E. F. et al. 2004, ApJ, 608, 752
Belloni, P. 1997, in Galaxy Scaling Relations: Origins, Evolution and Applications, ed. L. N. da Costa & A. Renzini, 319
Blake, C. et al. 2004, MNRAS, 355, 713
Blanton, M. R. et al. 2001, AJ, 121, 2358
Blanton, M. R., Lin, H., Lupton, R. H., Maley, F. M., Young, N., Zehavi, I., & Loveday, J. 2003, AJ, 125, 2276
Bohlin, R. C., & Gilliland, R. L. 2004, AJ, 127, 3508
Bolton, A. S. et al. 2012, AJ, 144, 144
Brotherton, M., Diamond-Stanic, A., vanden Berk, D., Burton, R., & Croom, S. 2004, in Astronomical Society of the Pacific Conference Series, Vol. 311, AGN Physics with the Sloan Digital Sky Survey, ed. G. T. Richards & P. B. Hall, 285
Brotherton, M. S. et al. 1999, ApJ, 520, L87
Bundy, K. et al. 2006, ApJ, 651, 120
Caldwell, N., Rose, J. A., & Dendy, K. 1999, AJ, 117, 140
Caldwell, N., Rose, J. A., Franx, M., & Leonardi, A. J. 1996, AJ, 111, 78
Cales, S. L. et al. 2011, ApJ, 741, 106
Chang, T.-C., van Gorkom, J. H., Zabludoff, A. I., Zaritsky, D., & Mihos, J. C. 2001, AJ, 121, 1965
Choi, Y., Goto, T., & Yoon, S.-J. 2009, MNRAS, 395, 637
Cortese, L., & Hughes, T. M. 2009, MNRAS, 400, 1225
Cushing, M. C., Vacca, W. D., & Rayner, J. T. 2004, PASP, 116, 362
Dawson, K. S. et al. 2015, ArXiv e-prints
—. 2013, AJ, 145, 10
Diamond-Stanic, A. M., Moustakas, J., Tremonti, C. A., Coil, A. L., Hickox, R. C., Robaina, A. R., Rudnick, G. H., & Sell, P. H. 2012, ApJ, 755, L26
Dressler, A., & Gunn, J. E. 1983, ApJ, 270, 7
Eisenstein, D. J. et al. 2001, AJ, 122, 2267
—. 2003, ApJ, 585, 694
—. 2011, AJ, 142, 72
Fan, X. et al. 1998, in Bulletin of the American Astronomical Society, Vol. 30, American Astronomical Society Meeting Abstracts, 1244
Fang, J. J., Faber, S. M., Koo, D. C., & Dekel, A. 2013, ApJ, 776, 63
Fang, J. J., Faber, S. M., Salim, S., Graves, G. J., & Rich, R. M. 2012, ApJ, 761, 23
Fukugita, M., Ichikawa, T., Gunn, J. E., Doi, M., Shimasaku, K., & Schneider, D. P. 1996, AJ, 111, 1748
Galaz, G. 2000, AJ, 119, 2118
Goto, T. 2004, A&A, 427, 125
—. 2005, MNRAS, 357, 937
—. 2007, MNRAS, 381, 187
Goto, T. et al. 2003, PASJ, 55, 771
Goto, T., Yagi, M., & Yamauchi, C. 2008, MNRAS, 391, 700
Gunn, J. E. et al. 1998, AJ, 116, 3040
Gunn, J. E., & Gott, III, J. R. 1972, ApJ, 176, 1

Gunn, J. E. et al. 2006, AJ, 131, 2332
Heymans, C. et al. 2012, MNRAS, 427, 146
Hogg, D. W., Masjedi, M., Berlind, A. A., Blanton, M. R., Quintero, A. D., & Brinkmann, J. 2006, ApJ, 650, 763
Hopkins, P. F., Hernquist, L., Cox, T. J., Di Matteo, T., Robertson, B., & Springel, V. 2006, ApJS, 163, 1
Hopkins, P. F., Hernquist, L., Cox, T. J., & Kereš, D. 2008, ApJS, 175, 356
Ivezic, Z. et al. 2008, ArXiv e-prints
Kauffmann, G. et al. 2003, MNRAS, 341, 33
Koranyi, D. M., & Strauss, M. A. 1997, ApJ, 477, 36
Krause, E., Hirata, C. M., Martin, C., Neill, J. D., & Wyder, T. K. 2013, MNRAS, 428, 2548
Leauthaud, A. et al. 2016, MNRAS, 457, 4021
Levi, M. et al. 2013, ArXiv e-prints
Lupton, R., Gunn, J. E., Ivezić, Z., Knapp, G. R., & Kent, S. 2001, in Astronomical Society of the Pacific Conference Series, Vol. 238, Astronomical Data Analysis Software and Systems X, ed. F. R. Harnden, Jr., F. A. Primini, & H. E. Payne, 269
Lupton, R. H., Gunn, J. E., & Szalay, A. S. 1999, AJ, 118, 1406
Madau, P., & Dickinson, M. 2014, ARA&A, 52, 415
Maraston, C. 2005, MNRAS, 362, 799
Maraston, C. et al. 2013, MNRAS, 435, 2764
Mihos, J. C., & Hernquist, L. 1994, ApJ, 431, L9
Miller, N. A., & Owen, F. N. 2001, ApJ, 554, L25
Miyazaki, S. et al. 2012, in Society of Photo-Optical Instrumentation Engineers (SPIE) Conference Series, Vol. 8446, Society of Photo-Optical Instrumentation Engineers (SPIE) Conference Series
Nielsen, D. M., Ridgway, S. E., De Propris, R., & Goto, T. 2012, ApJ, 761, L16
Norton, S. A., Gebhardt, K., Zabludoff, A. I., & Zaritsky, D. 2001, ApJ, 557, 150
Petrosian, V. 1976, ApJ, 209, L1
Poggianti, B. M. et al. 2009, ApJ, 693, 112
Poggianti, B. M., & Wu, H. 2000, ApJ, 529, 157
Pracy, M. B., Couch, W. J., Blake, C., Bekki, K., Harrison, C., Colless, M., Kuntschner, H., & de Propris, R. 2005, MNRAS, 359, 1421
Pracy, M. B., Couch, W. J., & Kuntschner, H. 2010, PASA, 27, 360
Pracy, M. B., Kuntschner, H., Couch, W. J., Blake, C., Bekki, K., & Briggs, F. 2009, MNRAS, 396, 1349
Pracy, M. B., Owers, M. S., Couch, W. J., Kuntschner, H., Bekki, K., Briggs, F., Lah, P., & Zwaan, M. 2012, MNRAS, 420, 2232
Quintero, A. D. et al. 2004, ApJ, 602, 190
Reid, B. et al. 2016, MNRAS, 455, 1553
Richards, G. T. et al. 2002, AJ, 123, 2945
Rubin, V. C., & Ford, Jr., K. W. 1986, ApJ, 305, L35
Salim, S., Fang, J. J., Rich, R. M., Faber, S. M., & Thilker, D. A. 2012, ApJ, 755, 105
Sandage, A., Tammann, G. A., & Yahil, A. 1979, ApJ, 232, 352
Sanders, D. B., Soifer, B. T., Elias, J. H., Madore, B. F., Matthews, K., Neugebauer, G., & Scoville, N. Z. 1988, ApJ, 325, 74
Schawinski, K. et al. 2014, MNRAS, 440, 889
Schechter, P. 1976, ApJ, 203, 297
Schlegel, D. J., Finkbeiner, D. P., & Davis, M. 1998, ApJ, 500, 525
Sell, P. H. et al. 2014, MNRAS, 441, 3417
Shin, M.-S., Strauss, M. A., & Tojeiro, R. 2011, MNRAS, 410, 1583
Sijacki, D., Springel, V., Di Matteo, T., & Hernquist, L. 2007, MNRAS, 380, 877
Smee, S. A. et al. 2013, AJ, 146, 32
Snyder, G. F., Cox, T. J., Hayward, C. C., Hernquist, L., & Jonsson, P. 2011, ApJ, 741, 77
Strauss, M. A. et al. 2002, AJ, 124, 1810
SubbaRao, M., Frieman, J., Bernardi, M., Loveday, J., Nichol, B., Castander, F., & Meiksin, A. 2002, in Society of Photo-Optical Instrumentation Engineers (SPIE) Conference Series, Vol. 4847, Astronomical Data Analysis II, ed. J.-L. Starck & F. D. Murtagh, 452–460
Swinbank, M., Balogh, M., Bower, R., Zabludoff, A., Lucey, J., McGee, S., Miller, C., & Nichol, R. 2011, ArXiv e-prints
Takada, M. et al. 2014, PASJ, 66, 1
The Dark Energy Survey Collaboration. 2005, ArXiv Astrophysics e-prints
Tran, K.-V. H., Franx, M., Illingworth, G., Kelson, D. D., & van Dokkum, P. 2003, ApJ, 599, 865
Tran, K.-V. H., Franx, M., Illingworth, G. D., van Dokkum, P., Kelson, D. D., & Magee, D. 2004, ApJ, 609, 683
Tremonti, C. A., Moustakas, J., & Diamond-Stanic, A. M. 2007, ApJ, 663, L77
Vacca, W. D., Cushing, M. C., & Rayner, J. T. 2003, PASP, 115, 389
Veilleux, S., & Osterbrock, D. E. 1987, ApJS, 63, 295
Vergani, D. et al. 2010, A&A, 509, A42
Whitaker, K. E., Kriek, M., van Dokkum, P. G., Bezanson, R., Brammer, G., Franx, M., & Labbé, I. 2012, ApJ, 745, 179
Wild, V. et al. 2014, MNRAS, 440, 1880
Wild, V., Heckman, T., & Charlot, S. 2010, MNRAS, 405, 933
Wild, V., Kauffmann, G., Heckman, T., Charlot, S., Lemson, G., Brinchmann, J., Reichard, T., & Pasquali, A. 2007, MNRAS, 381, 543
Wilson, J. C. et al. 2004, in Society of Photo-Optical Instrumentation Engineers (SPIE) Conference Series, Vol. 5492, Ground-based Instrumentation for Astronomy, ed. A. F. M. Moorwood & M. Iye, 1295–1305
Yagi, M., & Goto, T. 2006, AJ, 131, 2050
Yan, R. et al. 2009, MNRAS, 398, 735
Yan, R., Newman, J. A., Faber, S. M., Konidaris, N., Koo, D., & Davis, M. 2006, ApJ, 648, 281
Yang, Y., Zabludoff, A. I., Zaritsky, D., Lauer, T. R., & Mihos, J. C. 2004, ApJ, 607, 258
Yang, Y., Zabludoff, A. I., Zaritsky, D., & Mihos, J. C. 2008, ApJ, 688, 945
Yasuda, N. et al. 2001, AJ, 122, 1104
Yesuf, H. M., Faber, S. M., Trump, J. R., Koo, D. C., Fang, J. J., Liu, F. S., Wild, V., & Hayward, C. C. 2014, ApJ, 792, 84
York, D. G. et al. 2000, AJ, 120, 1579
Zabludoff, A. I., Zaritsky, D., Lin, H., Tucker, D., Hashimoto, Y., Shectman, S. A., Oemler, A., & Kirshner, R. P. 1996, ApJ, 466, 104